

An efficient RANS numerical model for cross-shore beach processes under erosive conditions

J. García-Maribona, J.L. Lara ^{*}, M. Maza, I.J. Losada

IHCantabria - Instituto de Hidráulica Ambiental de La Universidad de Cantabria, Isabel Torres 15, 39011, Santander, Spain

ARTICLE INFO

Keywords:

RANS
Sediment transport
Morphodynamics
Beach profile
CFD

ABSTRACT

In this work, a new numerical model for cross-shore beach profile evolution, IH2VOF-SED, is developed. It consists in the bidirectional coupling of a 2D RANS hydrodynamic solver and a sediment transport module. The resulting model is extensively validated against three benchmark cases at different scales, attending to the hydrodynamics, bottom shear stress and bathymetry evolution. Comparisons between experimental and numerical results show a good agreement for both the flow variables and the seabed evolution in all the validation cases without making use of calibration parameters. Additionally, the qualitative analysis of the results is in accordance with previous experimental observations of sediment transport induced by breaking waves. The computational cost is greatly reduced to about 1/10 of other available RANS models. As a novel aspect regarding RANS models, the model is able to simulate the swash zone and changes in the position of the coastline. A good compromise between precision and computational cost is achieved, allowing for an in-depth analysis of the processes leading to the cross-shore profile evolution.

1. Introduction

Processes related to nearshore sediment transport are typically classified, considering their temporal scales, into long-term (more than 10 years), mid-term (10 to 1 years), short-term (less than 1 year) and episodic (no fixed time scale). In particular, episodic events such as extreme storms can generate great damage to coastal structures or produce significant short-term erosion by modifying the beach profile. The way in which these events change the cross-shore beach profile has been studied using different approaches: semi-empirical, physical and numerical models as well as field observations.

Semi-empirical models can provide a prediction of the resulting beach profile for given hydrodynamic conditions. They can be classified into closed-loop and open-loop models depending on whether they consider that the equilibrium state is always achieved or not [Dean \(1995\)](#). Among the closed-loop approaches, the most common is [Bruun \(1962\)](#). For open-loop, different models have been proposed (such as [Miller and Dean \(2004\)](#), [Yates et al. \(2009\)](#), or [Jara et al. \(2015\)](#)). Semi-empirical models offer a relatively fast way to get results, although they require a specific calibration process for each application and the level of detail is not sufficient to reproduce important features such as breaker bars. Their main advantage is the reduced cost of application, that facilitates their use to predict mid and long-term variability of the cross-shore profile and the resulting shoreline.

Numerical modelling has been applied in nearshore hydrodynamics for a long time. Different hydrodynamic models are including sediment transport modules that allow them to solve the seabed evolution. The main advantages of numerical models are that they are generally cheaper than experimental set-ups and that they provide flexibility to easily adapt to new configurations. The most important drawbacks are the high computational cost of complex models and the lack of precision of the simpler ones, which can be problematic for certain applications as shown in [Kalligeris et al. \(2020\)](#). Numerical models have also been used in the research of nearshore morphodynamics, although their use for this purpose is not widely spread, because of difficulties in the correct simulation of the relevant processes.

Most of the simpler models calculate the mean flow due to different forces acting on the fluid without computing in-wave hydrodynamics. Rather, the wave effects are considered by including the radiation stress as a source term in their governing equations. In addition, the effects of wave breaking on the eddy viscosity or seabed shear stress can be included in the model by using different semi-empirical relations and parameters. The governing equations, used to compute the mean flow, can vary depending on the particular implementation. The most commonly chosen for this purpose are the Generalized Mean Lagrangian (GML) frame Shallow-Water Equations. A common way to compute the wave radiation stress is to solve the Wave Action Balance

^{*} Corresponding author.

E-mail address: lopezjav@unican.es (J.L. Lara).

Equation (as in Roelvink et al. (2009), Lesser et al. (2004)). In Nairn and Southgate (1993), the hydrodynamic model from Southgate and Nairn (1993) is used to compute the sediment transport produced by waves and currents. Other models resolve the in-wave hydrodynamics (and associated sediment transport). These are generally based on a Boussinesq model, for instance (Rakha et al., 1997). These simpler models show poor performance for the surf zone and require a large number of calibration parameters to achieve a good fit to the experimental results (as in Kalligeris et al. (2020)), greatly increasing the uncertainty associated with their predictions.

Among the most precise models that have been used to study the sediment transport are the RANS (Reynolds-Averaged Navier–Stokes) models. There are two main groups in which RANS models can be classified attending to the equations they solve. One-Phase models do not explicitly include the effect of sediment in the hydrodynamic equations, but it is implicitly included by changing the boundary conditions. In contrast, Two-Phase models include different sediment-related variables (such as the space occupied by it or the drag forces) in their governing equations. They can also be classified in Eulerian or Lagrangian depending on whether the control volumes used to compute the sediment transport are static or moving with the particles. Jacobsen et al. (2014) presents an Eulerian One-Phase RANS model that resolves the generation and development of a breaker bar under different wave conditions. Two-Phase Eulerian models (i.e. Cheng et al. (2017), Amoudry et al. (2005)) are generally too expensive to simulate the nearshore sediment transport processes. Therefore, they have been used for a more detailed analysis at small scale. Two-Phase Lagrangian models have been applied for similar purposes (for instance, Sun and Xiao (2016)). Other numerical studies address the nearshore hydrodynamics using RANS, but do not include the sediment transport (e.g.: Martins et al. (2017), Larsen et al. (2020)). These numerical models are able to accurately reproduce the hydrodynamics-sediment interaction and provide better quality results compared with the simpler ones, but at the cost of a high computational effort.

As discussed, each of the currently available techniques has its own limitations. These lead to gaps in the knowledge of cross-shore profile evolution, as some of the relevant aspects can hardly be studied with the approaches discussed above. For instance, the detailed evolution of the velocity or sediment flux fields would require very expensive numerical simulations or a great amount of measurements in the laboratory which could barely be acquired simultaneously. Furthermore, this translates into deficiencies in the predictive models, which are not able to reproduce some of the features of beach profile behaviour.

In this work, a new two-dimensional RANS numerical model, IH2VOF-SED, to simulate flow interaction with sediment transport and associated beach cross-shore processes is developed. In order to provide an accurate simulation of fundamental processes such as wave breaking or undertow generation, the hydrodynamic model IH2VOF is taken as a basis to incorporate sediment transport and seabed changes to the model. IH2VOF has been extensively tested and validated for surf zone hydrodynamics, showing high reliability and a low computational cost compared to other similar models. This has been considered an essential first step to achieve the objective of producing a new morphodynamic model able to provide reliable results of the relevant physical processes without compromising computational time, therefore overcoming some of the main limitations of existing models.

A complete description of IH2VOF-SED is provided in Section 2. Comparisons between experimental and numerical results for different benchmark cases are given in Section 3. Finally, the main conclusions are given in Section 4.

2. Numerical model description

IH2VOF-SED is based on a two-way coupling of a module solving the hydrodynamics and a sediment transport module. Consequently,

the hydrodynamics are inducing the sediment transport and the latter is affecting the hydrodynamics.

The hydrodynamic module uses a partial cell treatment to account for the effect of solid boundaries. These boundaries are displaced by the sediment transport module to achieve the aforementioned coupling. The partial cell treatment is convenient to account for the seabed displacement, as it does not produce any distortion in the computational mesh (in contrast with other strategies based on dynamic meshes like Farrell and Maddison, 2011). Hence, large variations in the seabed shape can be computed without generating numerical instabilities in the rest of the domain.

2.1. Hydrodynamic model

The hydrodynamic model used is IH2VOF (Lara et al., 2011; Losada et al., 2008). This model solves the RANS equations in 2DV dimensions by using the Finite Difference Method (FDM) in an orthogonal Cartesian staggered grid. To account for the effect of solid boundaries, a partial cell technique is adopted. The free surface tracking is performed by the Volume of Fluid method (VoF). The model can run in either laminar or turbulent conditions, using a $k - \epsilon$ turbulence model in the latter.

Governing equations. The governing equations for the hydrodynamics are the RANS equations. From mass balance in a control volume, the mass conservation equation for incompressible flows is

$$\nabla \cdot (\vec{U}) = 0 \quad (1)$$

in which \vec{U} is the mean velocity vector. The momentum conservation equations for incompressible and isotropic fluids are obtained from the momentum balance in a control volume, considering the total value of the velocity vector as the sum of the mean and fluctuating components.

$$\frac{\partial(\vec{U})}{\partial t} + \nabla \cdot (\vec{U} \otimes \vec{U}) = -\frac{\vec{\nabla} p}{\rho} + (\nu + \nu_t)\nabla^2 \vec{U} + \vec{S}_M \quad (2)$$

where p is the pressure, ρ is the fluid density, ν and ν_t are the molecular and turbulent viscosities and \vec{S}_M represents different body forces acting on the fluid. In this case, the only body force considered is the gravitational force.

The partial cell treatment is used to account for the effect of solid boundaries by considering the openness of the cell sides to the fluid (θ). Including this in Eqs. (1) and (2) they become

$$\nabla \cdot (\theta \vec{U}) = 0 \quad (3)$$

$$\frac{\partial(\theta \vec{U})}{\partial t} + \theta \nabla \cdot (\theta \vec{U} \otimes \vec{U}) = -\theta \frac{\vec{\nabla} p}{\rho} + \theta(\nu + \nu_t)\nabla^2 \vec{U} + \theta \vec{S}_M \quad (4)$$

The time derivative can be decomposed in

$$\frac{\partial(\theta \vec{U})}{\partial t} = \vec{U} \frac{\partial \theta}{\partial t} + \theta \frac{\partial \vec{U}}{\partial t} \quad (5)$$

The time derivative of the openness function in (5) represents the momentum added to the fluid as a result of boundary displacements. This term was added to the governing equations in Lara et al. (2011) to implement a virtual force method, and is further discussed in Mohd-Yusof (1997). However, in this case the variation of the openness function in time is very small and it can be considered that it does not add momentum to the fluid. Then, this term can be neglected leading to

$$\frac{\partial(\theta \vec{U})}{\partial t} \approx \theta \frac{\partial \vec{U}}{\partial t} \quad (6)$$

Therefore, (4) can be rewritten as

$$\frac{\partial(\vec{U})}{\partial t} + \nabla \cdot (\theta \vec{U} \otimes \vec{U}) = -\frac{\vec{\nabla} p}{\rho} + (\nu + \nu_t)\nabla^2 \vec{U} + \vec{S}_M \quad (7)$$

To obtain v_t , a turbulence closure model is needed. In this case, a $k-\epsilon$ model is used, which solves the transport equations for the turbulent kinetic energy (k) and its dissipation rate (ϵ). For each of these scalar fields, its transport equation considers the time variation and advective flux on the left-hand side and the diffusive flux, source and sink terms on the right-hand side. The turbulence model is based on Hsu et al. (2002), which incorporates a damping function in order to avoid the overproduction of turbulent kinetic energy addressed in (Larsen and Fuhrman, 2018).

$$\frac{\partial k}{\partial t} + \nabla \cdot (\vec{U}k) = \nabla \cdot \left[\left(\nu + \frac{\nu_t}{\sigma_k} \right) \vec{\nabla} k \right] - (\vec{u}^T \otimes \vec{u}^T) \vec{\nabla}(\vec{U}) - \epsilon \quad (8)$$

$$\frac{\partial \epsilon}{\partial t} + \nabla \cdot (\vec{U}\epsilon) = \nabla \cdot \left[\left(\nu + \frac{\nu_t}{\sigma_\epsilon} \right) \vec{\nabla} \epsilon \right] - C_{1\epsilon} \frac{\epsilon}{k} (\vec{u}^T \otimes \vec{u}^T) \vec{\nabla}(\vec{U}) - C_{2\epsilon} \frac{\epsilon^2}{k} \quad (9)$$

where σ_k and σ_ϵ are the Schmidt numbers for k and ϵ respectively. $C_{1\epsilon}$ and $C_{2\epsilon}$ are empirical coefficients. The values from (Wilcox, 1998) are

$$\sigma_k = 1.0; \sigma_\epsilon = 1.3; C_{1\epsilon} = 1.44; C_{2\epsilon} = 1.92 \quad (10)$$

Once k and ϵ are obtained, the turbulent viscosity can be calculated as

$$\nu_t = C_d \frac{k^2}{\epsilon} \quad (11)$$

where C_d is another empirical coefficient with a recommended value of $C_d = 0.09$.

The Volume of Fluid (VoF) method for free surface tracking consists in solving the advective transport of a magnitude representing the amount of fluid inside the cell. In contrast with other numerical models, which use the same strategy, IH2VOF does not solve the velocity, pressure and turbulent fields (k and ϵ) for the air phase. The equation for the advection of the VoF function F is

$$\frac{\partial F}{\partial t} + \nabla \cdot (\vec{U}F) = 0 \quad (12)$$

Solving algorithm. Aiming to solve the coupled velocity and pressure fields IH2VOF uses the Two-Step Projection method in which the FDM is used to obtain the expression of spatial derivatives for velocity and pressure fields in each cell. The system of equations which arises from the application of the Poisson Pressure Equation has a pentadiagonal coefficient matrix, in contrast with the system resulting from an unstructured mesh, which allows a more efficient solution of the pressure field. This system of equations is solved by using the Conjugate Gradient method preconditioned with an incomplete Cholesky factorization.

The transport Eqs. (12) for the VoF function and (8) and (9) for the turbulence model are solved explicitly using the FDM.

For further information about the solving method, the reader is referred to Lin and Liu (1998).

IH2VOF has been extensively validated for different hydrodynamic processes in the surf zone against both laboratory and field data (Lara et al., 2011; Torres-Freyermuth et al., 2007; Ruju et al., 2012).

2.2. Sediment transport model

The sediment transport is handled by a One-Phase Eulerian model which accounts for both bedload and suspended transport mechanisms. In addition, landslides are considered as a special type of bedload transport. Once these contributions are obtained, a mass balance is performed to obtain the seabed movement and, finally, the solid boundaries of the hydrodynamic model are updated by modifying the partial cell parameters.

The overall structure of the model is based on Roulund et al. (2005), although several aspects of the implementation have been changed to improve its behaviour and adapt it to the specific meshing strategy of the hydrodynamic model.

The inputs required by the sediment transport model are grain size, bulk density and porosity. The sediment fall velocity can be either specified by the user or estimated from the previous parameters using empirical formulae.

2.2.1. Bedload transport

Governing equations. Among the existing empirical methods that provide the instantaneous bedload transport rate (i.e. Bailard and Inman (1981), Stive (1986)), the one from Roulund et al. (2005) is selected as it has been previously used in Jacobsen et al. (2014) to successfully simulate the evolution of a beach profile, as well as in other sediment transport related problems such as Baykal et al. (2015) and Larsen et al. (2016). The sediment volumetric flux \vec{q}_b is calculated with

$$\vec{q}_b = \frac{1}{6} \pi d P_{ef} \vec{U}_b \quad (13)$$

in which d is the particle diameter, P_{ef} is the proportion of moving particles which depends on the difference between the Shields number and its critical value, and \vec{U}_b is the velocity of moving particles, obtained from the friction velocity. Further information about this method can be found in Roulund et al. (2005).

Eq. (13) is used for both friction-induced bedload transport and landslides.

Once the bedload transport is calculated its divergence is obtained, which represents the increment of sediment volume at each point of the fluid–sediment interface. This value is later considered to compute the variation of the seabed position.

Solving algorithm. To determine the bedload transport, the friction velocity must be obtained from the hydrodynamic model. The friction velocity (\vec{U}_f) is estimated considering a turbulent boundary layer with a logarithmic velocity profile:

$$\frac{\vec{U}}{\vec{U}_f} = \frac{1}{\kappa} \text{Ln} \left(\frac{y}{y_0} \right) \quad (14)$$

where \vec{U} is the velocity at a distance y of the solid boundary considered to be $y = 1.54\Delta y$, where Δy is the mesh discretization in the vertical direction of the corresponding cell, κ is the von Karman constant with a value of 0.41 and y_0 represents the shift of the velocity profile due to the boundary roughness. y_0 depends on the flow regime in the boundary layer, which can be divided in smooth (15)(a), transition (15)(b) and rough (15)(c) regimes:

$$y_0 = \begin{cases} \frac{0.11\nu}{|\vec{U}_f|}, & \text{if } \frac{k_s |\vec{U}_f|}{\nu} < 5 & \text{(a)} \\ \frac{0.11\nu}{|\vec{U}_f|} + \frac{k_s}{30}, & \text{if } 5 < \frac{k_s |\vec{U}_f|}{\nu} < 70 & \text{(b)} \\ \frac{k_s}{30}, & \text{if } \frac{k_s |\vec{U}_f|}{\nu} > 70 & \text{(c)} \end{cases} \quad (15)$$

where k_s is the Nikuradse roughness of the sediment, considered as 2.5 times the sediment diameter.

To avoid discretization problems inherent to the use of orthogonal grids with non-aligned boundaries, a method based on Capizzano (2011) to obtain the velocity vector close to the seabed is implemented. A similar approach was used in Lin et al. (2016) to interpolate velocities close to boundaries and later in Han and Lin (2018). The points in which the velocity is obtained are located at a distance of $1.54y$ in the normal direction with respect to the seabed, passing through the cell centroid (as shown in Fig. 1). The velocity components at this point are obtained for each seabed segment (u_i, v_i) by a bilinear interpolation weighted with the VoF function. The positions in which the hydrodynamic variables are calculated are represented in the left panel of Fig. 2.

Once the velocity components are obtained, the modulus of the velocity vector at the interpolation point is calculated. Then, the velocity vector is projected in the direction parallel to the seabed. The resulting velocity is inserted into (14) to obtain the friction velocity (\vec{U}_f). The friction velocity calculated in this way is continuous and smooth along the seabed. Once the friction velocity is known for each seabed cell, the different magnitudes needed to obtain the terms in (13) can be obtained.

Notice that, for smooth and transition regimes, the friction velocity appears also in the expression for y_0 and Eq. (14) cannot be solved directly. Instead, a Newton–Raphson algorithm is implemented to achieve an approximated solution for the friction velocity.

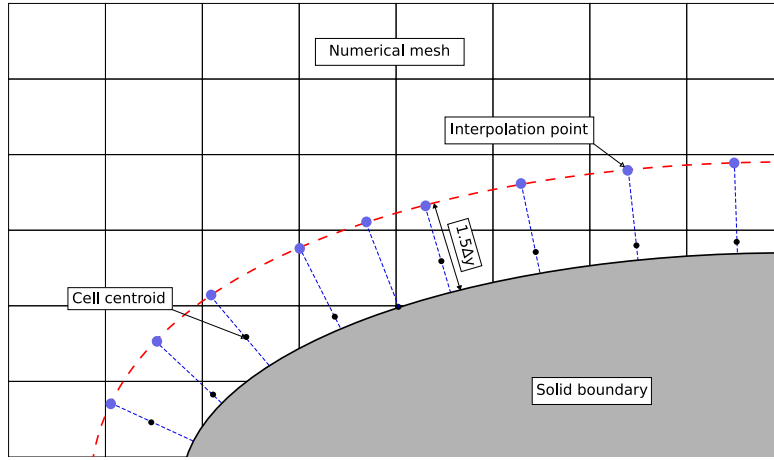


Fig. 1. Values for different magnitudes are calculated at interpolation points (blue dots). These are positioned at a distance $1.5\Delta y$ from the solid boundary (red line) and in a line normal to the wall surface (blue dashed lines) which passes through the cell centroid of the cell intersected by the wall surface (black dots).

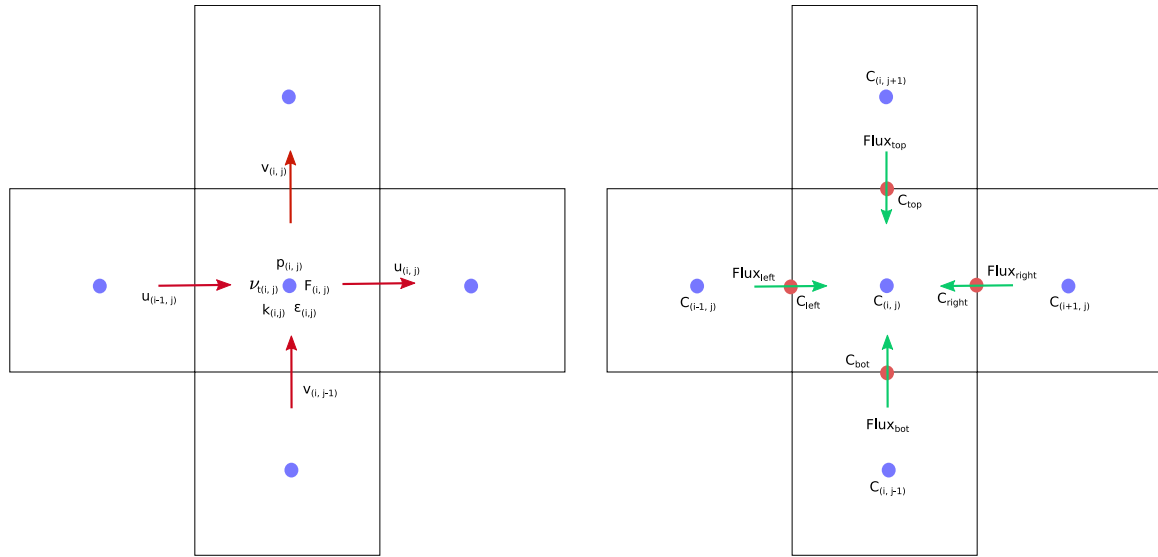


Fig. 2. Numerical stencil for hydrodynamic (left) and sediment (right) variables used in the model. Variables are calculated in the staggered grid for cell centres (blue dots) and faces (red dots). In the left panel, hydrodynamic variables (velocity, pressure, k , ϵ turbulent viscosity and VoF function), the velocity is represented with red arrows. In the right panel, the sediment module variables (sediment concentration in cell centre and interpolated to cell faces and sediment fluxes). The sediment fluxes are represented with green arrows, note the sign criteria for sediment fluxes (positive if entering the cell). (For interpretation of the references to colour in this figure legend, the reader is referred to the web version of this article.)

2.2.2. Suspended transport

Governing equations. In order to obtain the sediment interchange between fluid and solid, the sediment concentration field must be computed. This is done by solving the following advective–diffusive transport equation

$$\frac{\partial C}{\partial t} = \nabla \cdot [(\vec{U} + \vec{w}_s)C] + \nabla \cdot \left[\left(\frac{v + v_t}{\sigma_c} \right) \vec{\nabla} C \right] \quad (16)$$

where C is the sediment concentration. \vec{w}_s is the sediment fall velocity and σ_c is the Schmidt number for the sediment which was estimated between 0.5 and 0.7 in Amoudry et al. (2005). In this case, $\sigma_c = 0.5$ has been considered.

The magnitude of the sediment fall velocity can be provided as an input. In case it is not given, a default value based on the formulae from Fredsøe and Deigaard (1992) is used.

$$|\vec{w}_s| = \sqrt{\frac{4(s-1)gd}{3C_d}} \quad (17)$$

where s is the specific gravity of the sediment, g is the gravity acceleration, and C_d is the drag coefficient, obtained from the grain Reynolds

number as

$$C_d = 1.4 + \frac{36}{Re} \quad (18)$$

in which Re is the grain Reynolds number, obtained as

$$Re = \frac{w_s d}{\nu} \quad (19)$$

To avoid computing the sediment concentration distribution inside the boundary layer, the reference concentration (C_b) is used to estimate the concentration gradient at the boundary. The reference concentration and the elevation above the seabed level in which it occurs (a_{ref}) are obtained as proposed in Smith and McLean (1977). This formulation has been tested in Garcia and Parker (1991), providing the best results together with van Rijn (1984), and has the advantage for this application of giving the position of the reference concentration in terms of the Shields parameter, which is directly obtained from the friction velocity. Therefore, this strategy for the suspended transport boundary condition provides a relation between the suspended and bedload transport mechanisms.

Solving algorithm. The Finite Volume Method (FVM) is used to solve the advective–diffusive transport equation (16) in the spatial domain. The application of this method leads to an Ordinary Differential Equation (ODE) in the time domain. The resulting discretized advective–diffusive transport equation for each cell is (20)

$$\frac{\partial C}{\partial t} \approx \frac{\sum_n C_n (\vec{U}_n + w_{s,n}^-) A_n \theta_n + \sum_n \left(\frac{v+v_r,n}{\sigma_c} \right) \vec{\nabla} C_n A_n \theta_n}{V_{cell} \theta} \quad (20)$$

in which subscript n denotes values on the right, left, bottom and top faces of the cell. A_n is the face area, θ_n represents the openness of the cell face and V_{cell} is the cell volume. In the right panel of Fig. 2, the sediment fluxes of (16) are represented.

To compute the time-derivative of sediment concentration in each cell with Eq. (20), the cell face values of \vec{U} , w_s , C , v_t and $\vec{\nabla} C$ are needed. To determine these values, different interpolation and differencing schemes are used. A donor–acceptor interpolation scheme is used to compute the sediment concentration on cell faces to ensure mass conservation, which is discussed in Appendix A.

Spatial derivatives of sediment concentration at cell faces are obtained with a first order central difference scheme. However, for cells on the fluid–sediment interface, a boundary condition for the sediment fluxes must be applied in the solid part of their bottom faces. For the advective fluxes, a zero-gradient condition is prescribed. The condition for diffusive transport is a fixed gradient condition, which is approximated to avoid its expensive calculation. For this purpose, the concept of reference concentration is used, which assumes a layer of thickness a_{ref} and uniform concentration (C_b) around the solid boundary. The reference concentration is calculated using the aforementioned empirical formulae of Smith and McLean (1977).

The concentration field presents the same discretization problems as the velocity vector close to the seabed in the friction velocity equation, due to the use of an orthogonal mesh. For this reason, the concentration ($C_{i,j}$) used in (21) is interpolated with the same method followed to infer the velocity vector close to the wall (see Fig. 1). Furthermore, this value of sediment concentration close to the seabed is used to compute the advective flux in the lower boundary of the domain, which corresponds to the deposition rate.

Therefore, the concentration gradient between the point in which sediment concentration is interpolated and the solid boundary can be obtained as

$$(\vec{\nabla} C)_{b,i} = \frac{C_{interp,i} - C_{b,i}}{1.5\Delta y} \quad (21)$$

where $(\vec{\nabla} C)_b$ is the value of the concentration gradient for the boundary condition, C_{interp} is the interpolated value of the concentration field and C_b is the reference concentration obtained with Smith and McLean (1977). Subscript i th denotes the cell column. To determine the reference concentration ($C_{b,i}$), the Shields number obtained by the bedload transport module for the i th seabed segment is used.

The values of sediment fluxes on the seabed boundary constitute the interchange of sediment between fluid (suspended sediment) and soil. The deposition rate (\vec{D}) corresponds to the advective flux and the erosion rate (\vec{E}) to the diffusive flux. The expressions for the deposition and erosion rates are

$$\vec{D} = C_{interp} (\vec{U} + w_{s,bot}^-) A_{bot} \theta_{bot} \quad (22)$$

$$\vec{E} = (v + v_r) (\vec{\nabla} C)_b A_{bot} \theta_{bot} \quad (23)$$

where subscript bot denotes values on the bottom face of the cells.

Once all the terms in Eq. (20) are obtained, it is solved numerically using the 4th grade Runge–Kutta method for each cell in the domain. The sediment interchange across the fluid–sediment interface (erosion and deposition rates, \vec{E} and \vec{D}) has to be calculated in order to include it in the sediment balance and accordingly change the seabed shape. These rates are also obtained from the Runge–Kutta method.

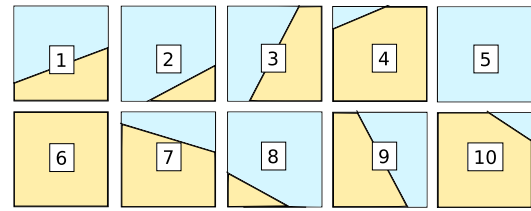


Fig. 3. Catalogue of considered cell types for the calculation of cell openness. An expression for $\theta_{i,j}$ and $\theta_{n,i,j}$ is obtained for each type.

2.2.3. Seabed movement

Governing equations. A sediment balance is performed for each cell in the fluid–solid interface. This balance computes the variation in the position of the interface, considering the bedload and suspended transport contributions, Δh_b and Δh_s respectively, to the total seabed displacement (Δh).

$$\Delta h_b = - \frac{1}{1 - e_d} \frac{\nabla \cdot (\vec{q}_b)}{\vec{e}_g \cdot \vec{N}} \Delta t \quad (24)$$

$$\Delta h_s = - \frac{1}{1 - e_d} \frac{|\vec{E} - \vec{D}|}{\vec{e}_g \cdot \vec{N}} \Delta t \quad (25)$$

$$\Delta h = \Delta h_b + \Delta h_s \quad (26)$$

where \vec{e}_g is the unitary vector in vertical direction, e_d is the sediment porosity and \vec{N} is the face normal vector, whose norm is equal to the face area.

Once the seabed movement is determined, the openness function values (θ and θ_n) for the cells must be updated in order to affect the hydrodynamics and achieve the bidirectional interaction with the sediment transport. The new values for θ and θ_n are determined purely by geometrical relations and then used in the next time step for the fluid motion calculation.

Solving algorithm. The previously described equations must be adapted taking into account the type of mesh that is used by IH2VOF. As it is an orthogonal grid based-on model, the product $\vec{e}_g \cdot \vec{N} = \Delta x_i$. Therefore

$$\Delta h_i = \Delta h_{b,i} + \Delta h_{s,i} = - \frac{1}{1 - e_d} \frac{\nabla \cdot (\vec{q}_b) + E_i - D_i}{\Delta x_i} \Delta t \quad (27)$$

Erosion, deposition and divergence of bedload transport are computed at the centre of each seabed segment, while the position of the interface (Y_{inter}) is defined at the sides of seabed segments. Consistently, a simple linear interpolation is used to translate segment–centre to segment–side values.

$$\Delta Y_{inter_{i+\frac{1}{2}}} = \frac{\Delta h_i + \Delta h_{i+1}}{2} \quad (28)$$

To determine the variation of the openness of a cell due to the new interface position, different geometrical relations can be deduced depending on the relative position of the interface and the cell faces. For this reason, a catalogue with all the possible configurations of the interface inside the cell is created. The geometrical relations to obtain the new openness of cell faces (θ_n) and volume (θ) are derived for each of them, assuming a linear fluid–solid interface inside the cell. The configurations taken into account are represented in Fig. 3. Therefore, each cell is classified using the catalogue and, then, the corresponding geometrical relations are applied to determine the openness of cell faces and volume. These parameters are used in the next time step by the hydrodynamic model.

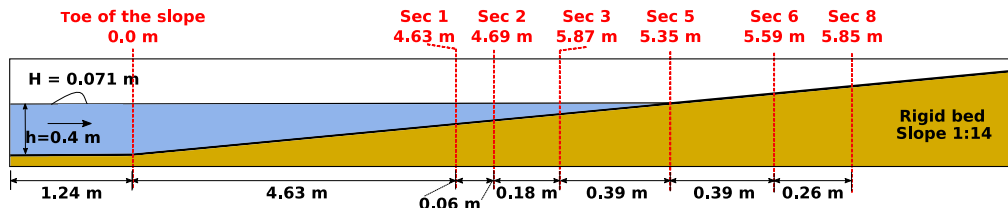


Fig. 4. Schematic view of the numerical domain and position of the sections where stresses and free surface are measured.

Table 1

Nondimensional numbers for the validation cases. Iribarren number (Ir_0), Dean parameter (Ω), Rouse number (P) and Shields number (ϕ).

Case	H (m)	T (s)	h (m)	d_{50} (mm)	w_s (m/s)	$\tan \alpha$	Ir_0	Ω	P	ϕ
Medium	0.43	3.7	2.50	0.25	0.034	1:15	0.47	3.42	3.1	0.14
Large	0.85	4.0	2.55	0.29	0.034	1:10	0.54	5.51	1.86	0.42

2.3. Solver parallelization

A great portion of the total computational cost of the model is associated with the resolution of the system of equations that provides the pressure values in the Two-Step Projection method. For this reason, the resolution of the system of equations has been parallelized to solve it in multiple CPU cores.

PETSc library (Balay et al., 2015b,a, 1997) has been used for this purpose. At the beginning of the simulation, the memory needed to store the coefficients matrix is allocated. The values of this matrix are updated every time step. Once the system of equations is solved and the new values of pressure obtained, the solution vector is gathered in the main processor which keeps performing the rest of computations.

A speed-up factor of approximately 1.75 has been achieved for the simulations, including hydrodynamics and sediment transport, when using an extra CPU core compared with the single-core version.

3. Validation and discussion

For the validation of the previously described numerical model, three experiments have been selected.

The first experiment (Sumer et al., 2013) consists in determining the shear stresses induced by a solitary wave breaking on a slope, responsible for the bedload transport and the dragging of sediment into suspension. The other two experiments, from Baldock et al. (2011) and van der Zanden et al. (2017b), consist in the evolution of a beach profile due to regular wave action. In all three cases, several complex processes encountered in the surf zone, such as wave breaking, reflection or the undertow, need to be modelled accurately. They are considered to be representative of the kind of problems for which the model will be applied. In addition, previous efforts to simulate the evolution of a complete beach profile using CFD models resulted in highly expensive computations and numerical instabilities in certain parts of the domain. The benchmark cases for beach profile evolution have been selected in order to have different scales (see Table 1).

The overall objective of this validation is to assess the ability of the model to reproduce the significant hydro-and morphodynamic processes occurring in the surf zone, as well as their interactions. Also, these validations provide an estimate of the computation costs and robustness of the model.

The computational costs of the validation cases are obtained for the simulations running on Intel i7-7700K CPU cores in both serial and parallel simulations

3.1. Friction velocity validation

The particular aim of the first validation case is to assess the ability of the model to reproduce the friction velocity (\bar{u}_f) generated by waves

on a beach profile, which is a key variable in sediment transport modelling. With this objective, the experiment presented in Sumer et al. (2011), performed on a fixed bed, is simulated numerically. The experiment consisted in a series of 7.1 cm high solitary waves breaking on a 1:14 slope covered with PVC plates to avoid erosion and water entrainment. The PVC plates were instrumented with hot film probes to measure the bottom shear stress. Free surface elevation was recorded using conventional resistive wave gauges. They were synchronized with the shear stress probes. Data from 7 sections are provided in Sumer et al. (2013) (see locations in Fig. 4). The first section is located at the toe of the beach and only wave height was measured at that position. Sections 1, 2 and 3 were located inside the shoaling zone, Section 5 at the still water level, separating the swash and surf zones, and Sections 6 and 8 in the swash zone (dry beach). The breaking point was located between sections 3 and 5. Several repetitions of the experiment were performed, allowing to obtain a statistical description of the solitary wave induced bottom shear stresses. In Sumer et al. (2013), the solitary wave breaking on the slope is divided in four stages: shoaling and breaking, run-up, run-down, and hydraulic jump and trailing wave. The same experiment is numerically reproduced in Li et al. (2019) and Larsen and Fuhrman (2019), the results from these works are also included in this validation for comparison with the present model.

For the numerical simulation, a solitary wave is generated 1.24 m from the toe of a 1:14 rigid bed slope, with a wave height equal to the one generated in the experiments and using Boussinesq theory. The mesh has a uniform discretization of $\Delta X = 0.0071$ m and $\Delta Z = 0.0035$ m, corresponding to an aspect ratio of 2, resulting in a total of 384,960 cells. A schematic view of the numerical set-up and the position of the sections used for the validation are given in Fig. 4.

A comparison between the experimental and the numerical results of free-surface evolution is shown in Fig. 5. As in the experimental results, $t = 0$ is considered as the instant when the wave crest is at the toe of the beach.

It can be observed that the free-surface is overall well predicted for the first two stages (shoaling and wave breaking and run-up, until $t = 3.0$). In the rundown and hydraulic jump stage the differences are more noticeable, particularly during the hydraulic jump (starting at 7.5 s). The trailing wave, which can be observed in the last part of the simulation at the toe section ($t = 10$ s approximately), is well modelled. The reason for the discrepancies in the hydraulic jump can be due to the three-dimensional and air entrainment effects, which are not accounted for in the model.

A comparison between experimental and numerical shear stresses induced on the seabed is presented in Fig. 6. Numerical bottom shear stresses are compared with the experimental ensemble-averaged stresses. The RMS (Root Mean Squared) of their fluctuations is also represented.

The results for the bed shear stresses provided by IH2VOF-SED can be compared to those of the aforementioned numerical models.

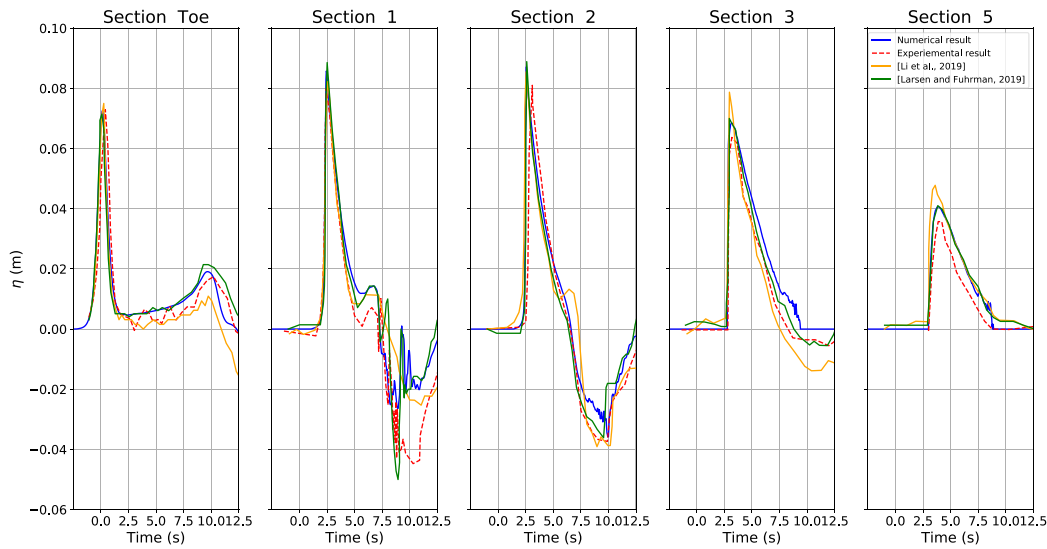


Fig. 5. Free-surface evolution recorded at the toe, and sections 1, 2, 3 and 5. Blue continuous line: numerical results from IH2VOF-SED. Orange continuous line: results from Li et al. (2019). Green continuous line: results from Larsen and Fuhrman (2019) Red dashed line: experimental results. (For interpretation of the references to colour in this figure legend, the reader is referred to the web version of this article.)

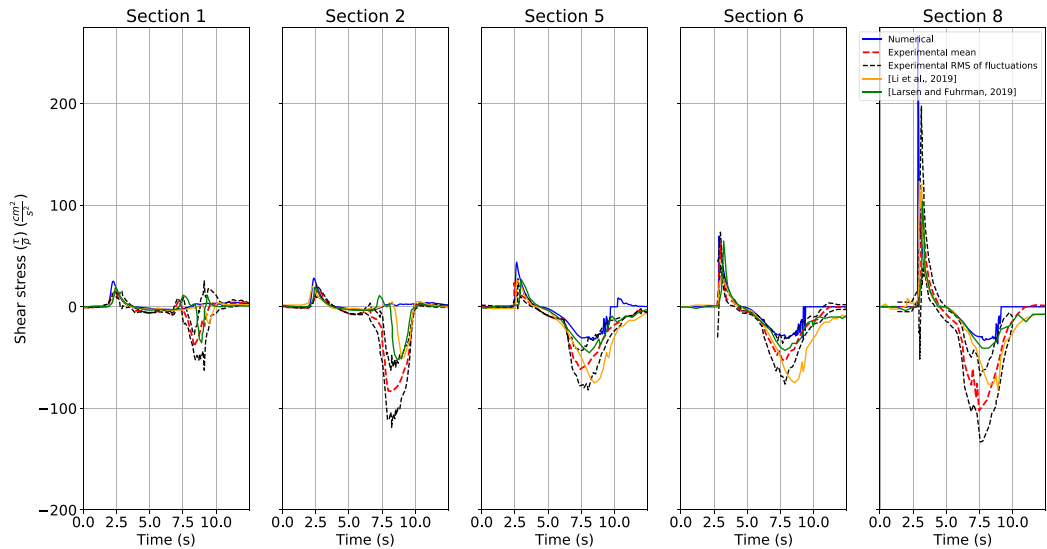


Fig. 6. Bottom shear stress evolution. Blue solid line: numerical results from IH2VOF-SED. Orange continuous line: results from Li et al. (2019). Green continuous line: results from Larsen and Fuhrman (2019). Red dashed line: mean shear stresses obtained in the experiment. Black dashed lines: RMS of the fluctuations added and subtracted from the experimental mean value. (For interpretation of the references to colour in this figure legend, the reader is referred to the web version of this article.)

In Li et al. (2019), a similar order of magnitude in the accuracy is achieved for the wave crest phase. The run-down is predicted also with a similar level of accuracy for sections 5, 6 and 8, while the result for Sections 1 and 2 are better than in IH2VOF-SED as their model is able to reproduce the negative (seaward) bed shear stresses. Larsen and Fuhrman (2019), provides a more accurate reproduction of the wave crest phase by adjusting the density of the cell in contact with the seabed instead of considering a fixed one. Whereas the accuracy of the results in sections 5, 6, and 8 is on the order of magnitude as IH2VOF-SED and Li et al. (2019), the wave trough phase is clearly better predicted for Sections 1 and 2, as Larsen and Fuhrman (2019) correctly reproduces the magnitude of the negative bed shear stresses.

It should be noted that the two models used as benchmark for IH2VOF-SED apply a body-fitted meshing strategy in contrast to the partial cell treatment used here. The former allows for a more accurate description of boundary layer effects but incurring in a higher computational cost, reported between two weeks and two months for Larsen and Fuhrman (2019) running in 12 Intel Xeon Processor ES-2680 v2

cores and one day for Li et al. (2019). With the present model, the simulation lasted for 1 h 45 min running in single-core.

As it was observed for the free surface measurements, the model predicts well the shoaling, wave breaking, initiation of the run-down and trailing wave for both the surf and swash zones. However, the shear stresses generated by the hydraulic jump are underestimated due to the aforementioned aspects. Note that this feature is enhanced in the case of a solitary wave compared to wind waves. Therefore, it is expected to have a reduced effect on the evolution of a beach profile. Thus, for the kind of problems that the model is intended to handle, the simplifications made in exchange for better efficiency can be considered to be acceptable.

Recalling that the friction velocity is directly related to the shear stress ($\bar{u}_f = \sqrt{\frac{\tau}{\rho}}$), the model can provide accurate predictions for it, as well as for the associated sediment transport features (bedload transport and amount of sediment put into suspension). It is also remarkable that the accurate prediction of the bottom shear stresses

extends to the swash zone, as can be observed in Sections 6 and 8 in Fig. 6.

3.2. Validation of beach profile evolution

The validation of beach profile evolution experiments specifically aims to confirm that the new model is able to predict the evolution of the seabed, as well as its interaction with the hydrodynamics, independently of scale.

Consequently, the validation of the cross-shore beach profile evolution is performed for two different scales. For the medium-scale validation, the experiment from Baldock et al. (2011) is selected. This experiment has been used previously as a validation case for the numerical model presented in Jacobsen et al. (2014). In fact, results in Jacobsen et al. (2014) are included as part of this validation since more precise boundary layer and turbulence treatment were implemented in the numerical model. However, at a very high computational cost. For the large-scale, the experiments from van der Zanden et al. (2017b) are selected, as they provide measurements of other relevant variables, such as velocities and sediment concentration.

The hydrodynamic and sediment conditions of the beach profile validation cases are summarized in Table 1. The nondimensional parameters which characterize the beach behaviour are the Iribarren number (Ir_0), Dean parameter (Ω), Rouse number (P) and Shields number (ϕ) (Grasso et al., 2009, 2011). These parameters are also given in Table 1 and are obtained as

$$Ir_0 = \frac{\tan \alpha}{\sqrt{\frac{H}{L_0}}} \quad (29)$$

$$\Omega = \frac{H}{w_s T} \quad (30)$$

$$P = \frac{w_s}{u'} \quad (31)$$

$$\phi = \frac{1}{2} f_w \frac{(A\omega)^2}{g \left(\frac{\rho_s}{\rho} - 1 \right) d_{50}} \quad (32)$$

where α is the angle of the offshore slope of the beach, H is the wave height on the paddle, L_0 is the wave length in deep water, w_s is the sediment fall velocity, T is the wave period, u' the turbulent fluctuation of the velocity, f_w the friction factor, A is the wave stroke close to the seabed and ω is the angular frequency of the wave

According to the Iribarren number, spilling breakers are expected for the medium-scale case and plunging breakers for the large-scale one. Regarding the Dean parameter (Ω), they correspond to intermediate beach states, being the large-scale closer to a dissipative state. In both of them a breaker bar formation is expected. The Rouse number is useful to characterize the surf zone and depends on the turbulence generated by wave breaking. The shoaling zone is driven by the Shields number. Rouse number and Dean parameter characterize the same physical processes (as explained in Wright and Short (1984)), as they represent the relation between the advective sediment transport due to turbulent motions and the sediment fall velocity, providing an estimation on the ability of turbulent motions to keep sediment in suspension. As these nondimensional parameters cover a wide range, the validation cases can be considered representative of the ability of the model to handle real beach configurations, despite the scaling of each individual experiment does not match any particular beach. Both validation cases of beach profile evolution are performed under monochromatic wave conditions.

The position along the beach profile (x) is normalized by the position and water depth associated with the breaking point (considered as the point in which the wave height starts decreasing). Therefore, the coordinate along the cross-shore profile is expressed as $\bar{x} = \frac{x-x_b}{h_b}$ where x_b is the breaking point position and h_b the water depth at that position. To facilitate the analysis and discussion of the results, the beach profile is divided into shoaling ($\bar{x} < 0$), outer surf ($0 < \bar{x} < 5$) and inner surf ($\bar{x} > 5$) zones according to Ting and Kirby (1994).

Unfortunately, some sediment properties are not given for the experimental cases in the corresponding literature. They are therefore estimated, although this may lead to some discrepancies between numerical and experimental results.

3.2.1. Medium-scale validation

The experiments from Baldock et al. (2011) were carried out in a 100 m long, 3 m wide and 5 m high wave flume at the Polytechnic University of Catalunya (UPC, Spain). The set-up consisted of a beach profile starting at 43 m from the wave paddle with a slope of approximately 1:15. Among the different wave conditions tested in the experiments, case named ME is selected for validation. Wave conditions were wave height $H = 0.43$ m, wave period $T = 3.7$ s, and water depth at the toe of the beach $h = 2.50$ m. Sediment characteristics were $d_{50} = 0.25$ mm and $w_s = 0.034$ m/s. More information about the grain size distribution used in this experiment is given in Cáceres et al. (2009), where it is reported that 92% of the grain size is between 0.15 and 0.35 mm. The seabed profile was obtained using a mechanical bed profiler after 24 min of waves.

The numerical simulations are performed considering 390 waves, consistently with the wave conditions reported by Baldock et al. (2011). Waves are generated at the left boundary of the numerical domain using Stokes II theory and active wave absorption. The beach slope of the numerical domain starts at 53.28 m from the position of the experimental wave paddle, with a 5.84 m long horizontal area to ensure that the generated waves can adapt to the water depth before getting transformed along the beach profile. The domain also includes part of the dry beach to ensure that the run-up does not reach the end of the domain. The final mesh has a total of 147.823 cells with $\Delta X = 0.038$ m and $\Delta Z = 0.019$ m. A mesh sensitivity analysis for this simulation is provided in Appendix B. Regarding the sediment properties, the nominal diameter and the sediment fall velocity were set according to the experimental data. The density is considered to be 2650 kg/m³ and the sediment porosity 0.40 (standard values for sand).

A schematic view of the numerical set-up is shown in Fig. 7.

The simulation, with morphological time of 2880 s (48 min), lasted 143 h (6 days) running on a single core and 93 h (less than 4 days) on two cores, without using any morphological acceleration factor. This represents a great reduction in the computational effort compared to the more complex model used for benchmarking. Jacobsen et al. (2014) reports that, for a case with a similar number of cells, it took one month to simulate 6000 s of morphological time considering a morphological acceleration factor of 5 and running in parallel using 4 cores. Notice that, using a morphological factor of 5, the same simulation using IH2VOF-SED would take 44 h in a single core or 25 h using two cores.

In Fig. 8, the bathymetry after 24 and 48 min of simulation (390 and 780 waves approximately) is compared with results from the experiment, XBeach (using default parameters) and the model from Jacobsen et al. (2014). Only the part of the domain where significant changes in the bathymetry occurred is shown.

Laboratory and numerical results from IH2VOF-SED are displayed in Fig. 8 corresponding to 24 min and 48 min of wave action. In both, laboratory and experiment, a breaker bar and trough are generated in the same position initially, and they migrate offshore between minutes 24 and 48. The main differences are in the size of the trough and the secondary breaker bar (at $\bar{x} = 10$). Regarding the swash zone, the erosion is correctly reproduced.

There are various potential sources for the discrepancies between IH2VOF-SED and the experimental results. Firstly, the three-dimensional nature of the breaking process and the influence of the air entrainment are not accounted for in the numerical model, neither are the effects of the grain size distribution in sediment transport. Additionally, some non-uniformity of the profile across the wave flume is reported in Baldock et al. (2011). Furthermore, differences regarding the exact conditions in which the experimental and numerical simulations were performed, such as the wave generation/absorption system

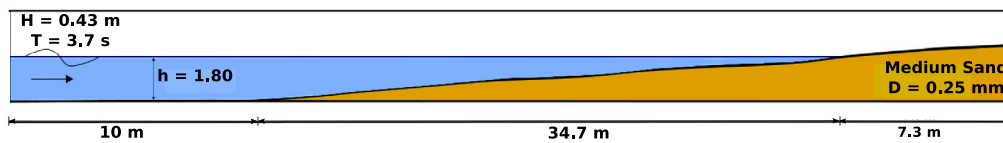


Fig. 7. Schematic view of the numerical domain.

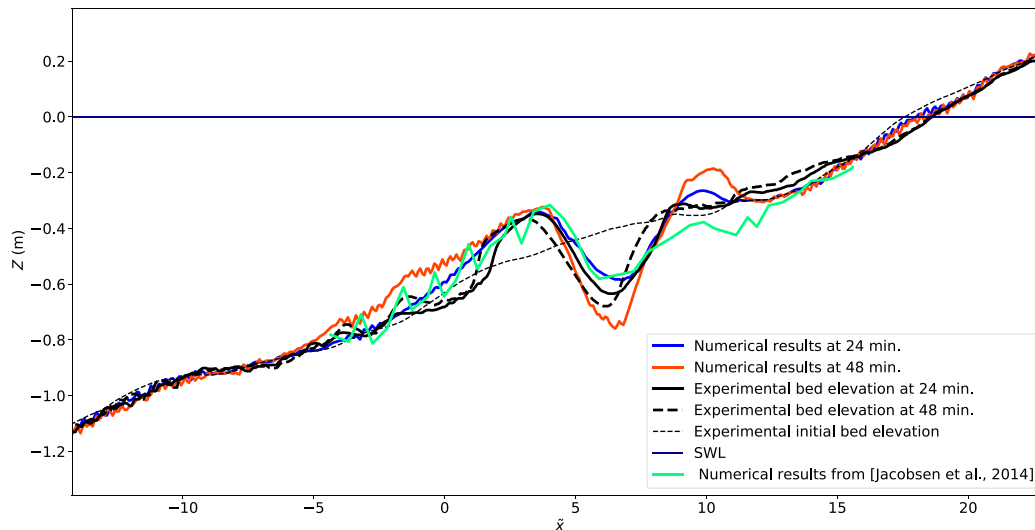


Fig. 8. Resulting bathymetry after 24 and 48 min of waves. Blue line: IH2VOF-SED after 24 min. Red line: IH2VOF-SED after 48 min. Green line: numerical results from Jacobsen et al. (2014) after 23 min. Orange line: XBeach (default parameters) after 24 min. Black dashed line: initial bed level. (For interpretation of the references to colour in this figure legend, the reader is referred to the web version of this article.)

and sediment properties, can lead to the aforementioned discrepancies. In particular, the uncertainty in the exact position of the initial and final seabed can be responsible for the differences in the depth of the trough. The mechanical device used to measure the position of the seabed in Baldock et al. (2011) had a limited precision, and systematically measured the position of the trough of the ripples. By performing a mass balance with the provided experimental results, it can be observed that there is an excess of erosion of around 0.5 m^3 per metre of width. As discussed in Baldock et al. (2011), this excess of erosion cannot be directly imputed to a certain region of the beach profile. Finally, the precision of the empirical formulae included in the model also limits its overall performance.

A comparison of the cross-shore beach profile results obtained from IH2VOF-SED, XBeach and Jacobsen et al. (2014) for the 24 min profile is performed. The numerical model presented in Jacobsen et al. (2014) provides a similar prediction of the position of the breaker bar and trough, and large erosion in the inner surf zone, while in the present model the later does not suffer significant changes. The computational cost in which the model from Jacobsen et al. (2014) incurs to simulate some features of the hydrodynamics is much higher than the present model for the simulation of a significantly smaller domain. The main reason for this is the different types of meshing strategy followed by each model. While IH2VOF-SED uses a orthogonal structured mesh, Jacobsen et al. (2014) uses an unstructured meshing strategy. The former provides substantial advantages in terms of computational cost, as the system of equations being solved in the Two-step Projection Method has a pentadiagonal matrix in contrast with the sparse matrix arising from the use of unstructured meshes. However, unstructured meshes can easily adapt to the solid shapes while IH2VOF-SED relies on the, less precise, partial cell treatment for this purpose. In addition, as reported in Jacobsen et al. (2014), numerical instabilities due to the combination of air and water in a thin layer required an upper cut-off of the beach profile eliminating the swash zone to be able to run the simulations. The difficulties to numerically simulate the swash zone are also pointed

in van Rijn et al. (2011). The elimination of the swash zone implies that some of the hydrodynamic processes could be affected. For instance, the balance between onshore/offshore-directed mass and linear momentum fluxes, key aspect for the generation of the undertow current in the surf zone, can be altered by this simplification. Furthermore, sediment which can be potentially eroded and transported to the breaker bar (and viceversa) is not accounted for, and the morphological effects that result from this interaction, such as beach accretion, may not be reproduced. Finally, a morphological acceleration factor was used to perform the simulations, which can also affect the resulting bathymetry.

Regarding the results from XBeach, they are clearly deviated from the laboratory results. The breaker bar and trough are not generated. Instead, a general erosion in the shoaling and surf zones is predicted. The main accumulation of sediment occurs in the inner surf zone.

In order to quantify the ability of each model to correctly reproduce the evolution of the beach profile, the Brier Skill Score (BSS) is used. As the BSS uses the difference between initial and final observed profiles, the aforementioned excess of erosion in the final laboratory profile must be compensated. As the excess of erosion cannot be directly imputed to a certain part of the profile, this is done by adding a uniform shift on the final profile of 8 mm. The skill score is calculated for the same domain simulated in Jacobsen et al. (2014) so that the three models can be compared. The obtained values are -0.21 for XBeach, 0.75 for IH2VOF-SED and 0.42 for Jacobsen et al. (2014). According to van Rijn et al. (2003), the performance of the models can be classified as bad ($BSS < 0$) for XBeach, reasonable for Jacobsen et al. (2014) ($0.30 < BSS < 0.60$) and good for IH2VOF-SED ($0.60 < BSS < 0.80$). If the same comparison is performed for the complete beach profile, including the shoaling and swash zones, the results are -0.23 for XBeach and 0.73 for IH2VOF-SED, results for Jacobsen et al. (2014) cannot be obtained as the simulated domain did not cover these areas. After 48 min of simulation, the BSS for IH2VOF-SED is 0.30 (reasonable).

Using IH2VOF-SED only, the evolution of the seabed shape along the simulation is displayed in Fig. 9.

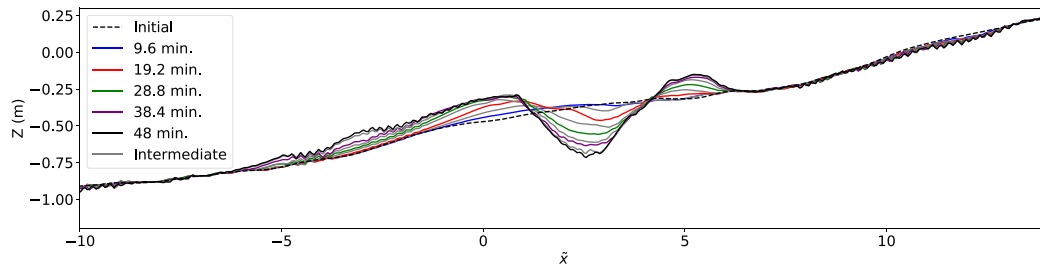


Fig. 9. Mean seabed shape at different instants along the simulation. Black dashed line: initial seabed. Blue line: after 9.6 min (155 waves). Red line: after 19.2 min (311 waves). Green line: after 28.8 min (467 waves). Purple line: after 38.4 min (622 waves). Black line: after 48 min (778 waves). Grey lines: intermediate profiles each 4.8 min (78 waves). (For interpretation of the references to colour in this figure legend, the reader is referred to the web version of this article.)

There is an initial growth of the breaker bar produced by the sedimentation of sand eroded from the shoaling, surf and swash zones. The trough is generated mainly after 9.6 min, once the breaker bar has acquired a sufficient size to significantly affect the hydrodynamics. The breaker bar grows in the same place until minute 19.6 approximately. Later, it starts migrating offshore (minutes 19.6 to 38.2). For the last interval (minutes 43.2 to 48), it can be noted that the breaker bar stops migrating and the bar trough does not deepen any further, reaching a pseudo-equilibrium status. This behaviour is observed in both, the experiment (not shown) and the numerical simulation.

The contribution of each sediment transport mechanism to the bathymetry changes can be also extracted from the model according to Eqs. (24)–(26). These contributions are shown in Fig. 10

As can be noted, both the bedload and suspended contributions tend to erode the position of the bar trough and to accumulate sediment where the breaker bar is generated. At the beginning of the simulation, the zone in which the suspended transport accumulates sediment starts close to the wave breaking point (at $\bar{x} = -1$) and extends until the plunge point ($\bar{x} = 3$ approximately). The bedload contribution accumulates sediment on a reduced area ($2 < \bar{x} < 3$), leading to the growth of the onshore side of the breaker bar. As the simulation advances, both transport contributions produce erosion in the bar trough, and the suspended contribution is shifted offshore with respect to the bedload component. It can also be noted that the zones where sediment is accumulated by both mechanisms are displaced offshore as the simulation progresses (more remarkably in the case of the suspended contribution, from $-1 < \bar{x} < 3$ to $-5 < \bar{x} < 0$). This results in the migration of the breaker bar shown in the bathymetry evolution of Fig. 9. Close to the end of the simulation, both time-averaged contributions are smaller, and they compensate each other on top of the breaker bar ($\bar{x} = 1$) and, partially, in the bar trough ($\bar{x} = 3$) as the beach profile approaches the pseudo-equilibrium status.

In Fig. 11, the evolution of wave height, friction velocity, bedload and suspended sediment transports and bathymetry are shown.

Panels A and B in Fig. 11 show that the net friction velocity is positive seaward of the breaking point and changes its sign in the surf zone, approximately at the breaking point ($\bar{x} = 0$). This can be explained considering the mean velocity distribution along the beach profile (shown in Fig. 12). It can be observed that the peak in negative friction velocity occurs at the position where the trough is generated ($\bar{x} = 2.5$ approximately). The near-bed mean velocity is onshore-directed in the shoaling zone, due to the asymmetry of shoaling waves and steady streaming, and offshore-directed in the surf zone, due to the undertow. This is a well-known feature, on which many simpler numerical models rely to predict the resulting beach profile (i.e. Hoefel and Elgar (2003)). However, after the breaker bar is generated, an onshore-directed friction velocity appears in the bar trough, consistent with the high friction velocities induced by the breaking process (when the plunging jet reaches the seabed). The effect of this high instantaneous velocity is also reflected in Fig. 12 panel D, where a small area of near-bed onshore-directed mean velocity can be spotted between $\bar{x} = 3$ and $\bar{x} = 5$. This same feature is shown in some laboratory

data (e.g. Okayasu and Katayama (1992)). In panel C, the bedload transport follows the same trend as the friction velocity, consistently with Eq. (13). The suspended transport, shown in panel D, produces erosion in the shoaling zone and part of the surf zone (initially for $\bar{x} < 5$). The eroded sediment is deposited mainly around the breaking point at the beginning of the simulation, resulting in the generation of the breaker bar. For the last time interval, a significant change in the suspended transport trend can be observed, the sediment is no longer deposited at the breaker bar position but rather on its offshore slope, effectively inhibiting further growth of the breaker bar and producing offshore migration as discussed in Fig. 10. The mean seabed shape for every interval is represented in panel E for reference.

One of the main drivers of the cross-shore profile evolution is the undertow. To examine its variation along the simulation due to the interaction with the changing seabed, the time-averaged horizontal velocity field is represented in Fig. 12.

The undertow can be clearly identified as the blue areas (offshore-directed velocities in Fig. 12). The red coloured areas correspond to onshore-directed mean velocities. For the initial situation (panel A) the maximum undertow occurs offshore the plunge point (where the plunge jet impinges the water, at $\bar{x} = 3.0$ approximately), coinciding with the maximum onshore-directed mass flux produced by breakers, and weakens as it moves into the shoaling zone. In the subsequent panels, the maximum value occurs at a larger distance seawards of the plunge point, the value right at the plunge point close to the seabed even becomes positive in the last intervals (panels C and D, can also be noted in Fig. 11 panel B). It can be observed that, seawards of the breaking point, the undertow is being enhanced as the breaker bar develops. Another aspect that can be noted is the undertow detachment from the seabed. The detachment point (where the near-bed velocities change their sign, being offshore directed in the onshore side and onshore directed in the seaward side) is also displaced offshore as moving from panel A to D. This can be quantitatively observed in panel B of Fig. 11, where the point in which the mean friction velocity changes its sign is displaced offshore for the first 400 waves.

A key aspect in the generation of the breaker bar is the correct simulation of sediment fluxes induced by the breakers. To further analyse this aspect, the instantaneous sediment fluxes and concentration fields for different time instants during wave breaking are represented in Fig. 13, together with the instantaneous friction velocities.

Panel A shows a shoaling wave approaching the break point. The suspended sediment transports resulting from the wave crest passing (onshore directed) and the undertow current (offshore directed), meet at $\bar{x} = -2$ approximately. Panel B displays the instant when wave breaking starts ($\bar{x} = -1.0$). The sediment transported by the previous mechanisms is accumulated in the wave front ($\bar{x} = -0.5$). The instant when the plunger jet impinges the water is displayed in Panel C. It can be observed that a large eddy is generated at $\bar{x} = 2.0$. This eddy produces a great mixing of sediment. Finally, panel D displays how the large eddy breaks into several smaller ones (roughly at $\bar{x} = 2.25, 3.25, 5.5$), that occupy the available water depth, further mixing the upper and lower layers of the surf zone. The mixing effect of these

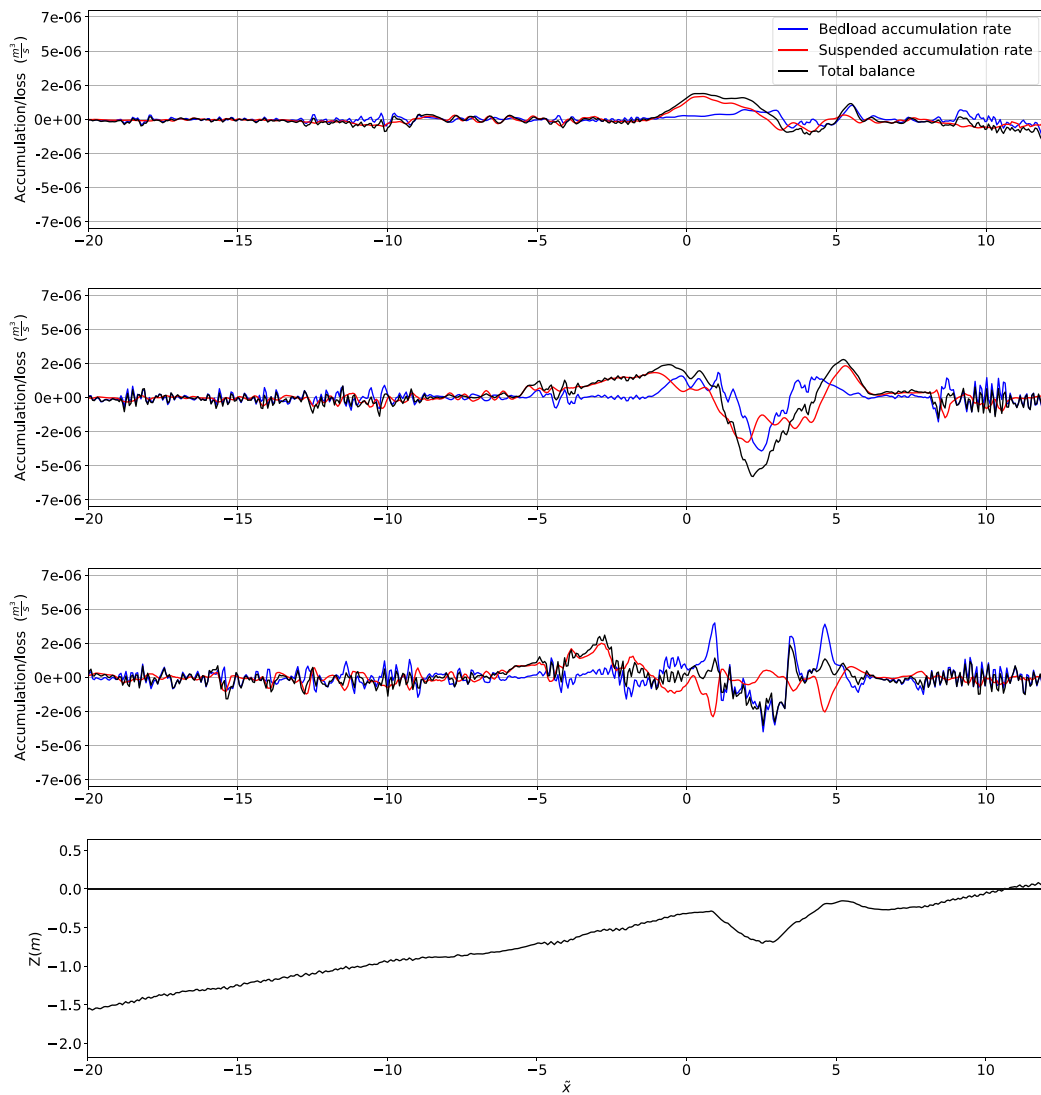


Fig. 10. Contributions of the bedload and suspended transport mechanisms to the bathymetry changes. Panel A: waves 0 to 100. Panel B: waves 300 to 400. Panel C: waves 600 to 700. Panel D: Bathymetry after 700 waves.

eddies also enhances the momentum transfer between upper and lower layers, resulting in a reduction of the undertow velocity for the inner surf zone in accordance with Ting and Kirby (1995).

The sediment concentration and flux patterns shown in Fig. 13 are in agreement with qualitative experimental observations, as the ones given in Sumer et al. (2013).

3.2.2. Large-scale validation

The experiments used for the large-scale validation were conducted in the UPC laboratory, in the same flume used for the medium-scale validation test. In this case, an initial position of the breaker bar was obtained in the first run. Then, several runs tracking the evolution of the breaker bar and measuring hydrodynamic parameters were conducted starting with the same initial profile, which was recovered after each run. Wave conditions in this case were $H = 0.75$ m at the toe of the beach (reportedly 0.85 m at the generation), $T = 4$ s and $h = 2.55$ m at the wave-maker. A total of 450 waves (1800 s) were generated. Sediment grain size was $d_{50} = 0.29$ mm with $d_{90} = 0.42$ mm and $d_{10} = 0.19$ mm, and its fall velocity equal to 0.034 m/s. The wave height was measured using resistive wave gauges. For the velocities, ADVs were located at different positions to obtain velocity profiles. Regarding sediment concentration, Transverse Suction System nozzles (TSS) and Optical Backscatter Sensors (OBS) were used for the outer

flow, while Acoustic Concentration and Velocity profilers (ACVP) were used close to the seabed.

For this validation, the evolution of the breaker bar, starting from the same initial profile as the one in the experiments, is numerically reproduced. The averaged beach profile and its top and bottom bounds, obtained by adding and subtracting the standard deviation of the results, are compared with the numerical results.

In the experimental set-up, the foreshore ($\bar{x} > 13.0$) was protected by a geotextile. This feature is introduced in the numerical simulation as an immobile-bed boundary condition. Waves are generated using Stokes II theory and active wave absorption. The sediment nominal diameter and fall velocity are set according to the experiments. Sediment porosity is set to 0.40 (standard value for a loosely packed bed) and the sediment density is considered to be 2650 m^3/s . The mesh consisted of 127,300 cells considering $\Delta X = 0.058$ m and $\Delta Z = 0.029$ m. The influence of mesh discretization is discussed in Appendix B. A schematic description of the numerical domain, including the position of the different gauges that are used for the validation, is shown in Fig. 14. The simulation took 57 h running in single core and 33 h in two cores.

The numerical results are compared to the experimental data. The position and depth of the breaking point provided in van der Zanden et al. (2017b) are used to normalize the results. Numerical results of

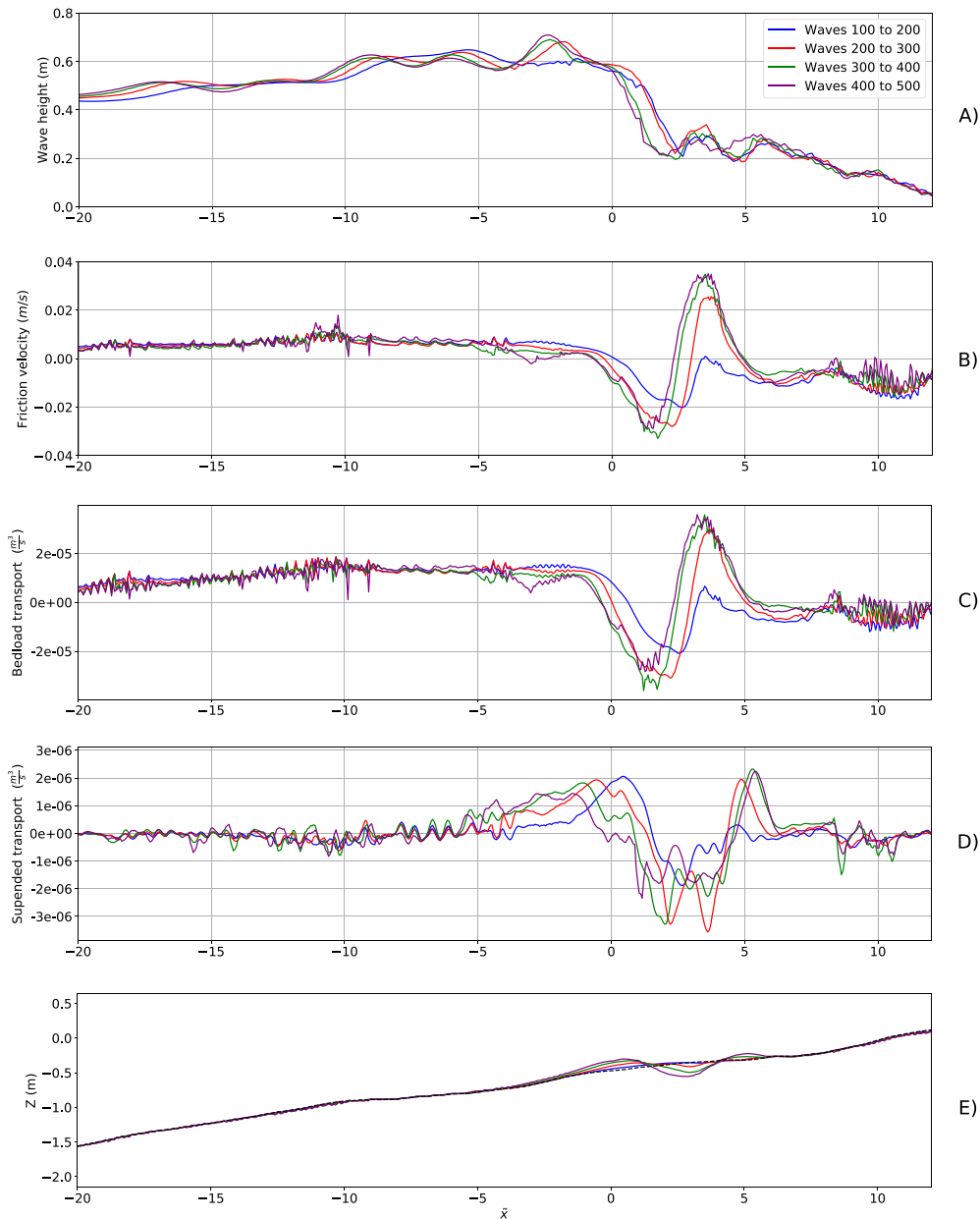


Fig. 11. Evolution of wave height, friction velocity, bedload and suspended transports and resulting bathymetry. Blue line: waves 100 to 200. Red line: waves 200 to 300. Green line: waves 300 to 400. Purple line: waves 400 to 500. In the bottom panel, the initial bed elevation is displayed in black dashed line. (For interpretation of the references to colour in this figure legend, the reader is referred to the web version of this article.)

wave height along the cross-shore profile, obtained as the mean value between waves 50 and 100, are compared to the experimental data in Fig. 15.

The evolution of the wave height along the cross-shore profile shows a good agreement with the experimental results, as observed in Fig. 15. It can be noted that the mean wave height coincides at the generation boundary, shoaling, outer and inner surf zones. Also, the position of the breaking point (where the drop in wave height starts) has been accurately reproduced by the model as it is located at $\bar{x} = 0$.

The phase-averaged free surface at different positions along the profile is also compared with experimental data, it has been obtained for 50 waves after 200 s of regularization time. Fig. 16 shows this comparison.

Fig. 16 shows an overall good agreement between the numerical and the experimental data. Close to the wave generation, the differences are more noticeable (panel A left). The differences vanish close to the breaking point (panels A right and B left). Onshore of the breaking point

(panels B right, C left and C right) the numerical results are also in good agreement with the experimental ones.

The comparison between numerical and experimental results for phase-averaged velocities at different points in the domain is also performed and shown in Fig. 17. Five positions along the cross-shore profile are presented. Row A corresponds to the onshore part of the shoaling zone, very close to the breaking point. Rows B, C and D correspond to different positions in the outer surf zone and row E to a position in the inner surf zone. For each position along the profile three points are measured in the vertical. The first column in Fig. 17 corresponds to measurements close to the seabed. The second column displays results for a position at approximately half of the water depth, and the third column shows results close to the free surface. The coordinate Z represents the distance from the bottom of the channel ($Z = 2.55$ m for the still water level). Again, the phase-averaged values are obtained for 50 waves after 200 s of simulation.

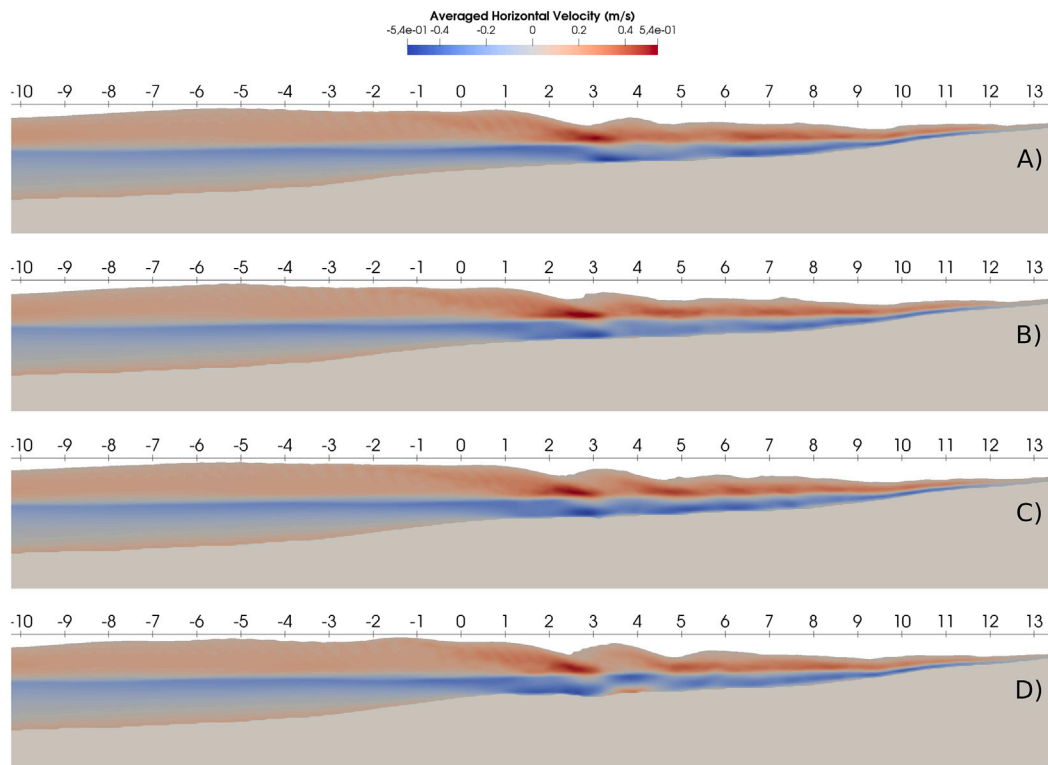


Fig. 12. Time-averaged horizontal velocities obtained for different wave intervals. Panel A: waves 50 to 60. Panel B: waves 100 to 110. Panel C: waves 150 to 160. Panel D: waves 200 to 210. The wave envelope and seabed shape are represented by white lines. Negative velocities are offshore-directed. (For interpretation of the references to colour in this figure legend, the reader is referred to the web version of this article.)

As can be observed in Fig. 17, numerically obtained velocities are in good agreement with the experimental results. The outer surf zone (particularly rows B and C) presents the most noticeable differences. The shoaling zone (row A) and inner surf zone (row D) show good agreement between the numerical and the experimental data, although the mean velocity is slightly overestimated. An underprediction of the undertow velocity could be the reason for this deviation.

The numerical and experimental mean sediment concentration profiles at different positions along the beach profile are also compared. Fig. 18 shows the numerical and experimental averaged concentration profiles, obtained for 50 waves after 400 s of simulation.

Fig. 18 shows a reasonable overall agreement between experimental and numerical results. For the shoaling region, close to the breaking point, and initial part of the outer surf zones (until $\bar{x} = 2.7$ approximately) the differences are more noticeable as the model over-predicts the sediment concentration, with a Root Mean Square Error (RMSE) between 6.2 and 9.8 kg/m³, while for the rest of the outer surf zone and inner surf zone the results are very close to the experimental measurements, with a RMSE of 0.17 to 1.9 kg/m³.

The differences between experimental and numerical results in the surf zone are of the same order of magnitude as the results provided by the empirical formulae used to compute the entrainment of sediment into suspension (see García and Parker (1991)). Therefore, the accuracy of the formulae could be responsible for a significant part of the differences between experimental and numerical concentration profiles in the surf zone. For the shoaling zone and the beginning of the outer surf zone, a low concentration gradient close to the seabed is responsible for the poor agreement. This low concentration gradient can be due to an overestimation of the near-bed mixing processes (vertical velocities and turbulence) produced in the initiation of the wave breaking. Additionally, it should be kept in mind that the near-bed concentration measurements have a high level of uncertainty, according to van der Zanden et al. (2017a). The aforementioned underprediction of the undertow velocities, which results in larger velocities during the crest

phase (as shown in Fig. 17), also leads to a larger volume of sediment put into suspension in the inner surf zone.

Finally, the resulting beach profile after 30 min of simulation (450 waves) is compared with the experimental measurements in Fig. 19.

Fig. 19 shows that the experimental and numerical results are close to each other. The main difference is the excessive growth of the breaker bar obtained with the numerical model in comparison with the experimental data. This discrepancy can be explained by the excessive concentration put in suspension shown in Fig. 18, which results in more rapid variations of the seabed. There is also a small landwards shift in the bar position which is associated with the underestimation of undertow velocities commented in Fig. 17, leading to an increase in the onshore sediment transport. However, the quantitative evaluation of the performance of the numerical model for the region around the breaker bar ($\bar{x} = -2$ to $\bar{x} = 6$), gives a Brier Skill Score (BSS) of 0.07 for the numerical results, which is classified as “poor” (slightly better than the null hypothesis) according to van Rijn et al. (2003). Comparing this value to that of the medium-scale validation case, also obtained in the breaker bar region, (0.75 for IH2VOF-SED) this seems to be a low value. In this regard, it should be kept in mind that in the large-scale validation case the small variations of the initial bathymetry, in which the breaker bar is already present, make the comparison with numerical results more unfavourable. If compared to a null hypothesis of an unbarred initial profile (as in the medium scale validation), the difference between experimental results and null hypothesis would be larger, and the BSS for the numerical model better. Unfortunately, the authors do not have access to the shape of the experimental beach profile before the breaker bar was generated to compute this quantity.

4. Conclusions

In this work, a new numerical model capable of solving the cross-shore beach profile evolution, IH2VOF-SED, is developed. The model offers a unique compromise between precision and computational cost.

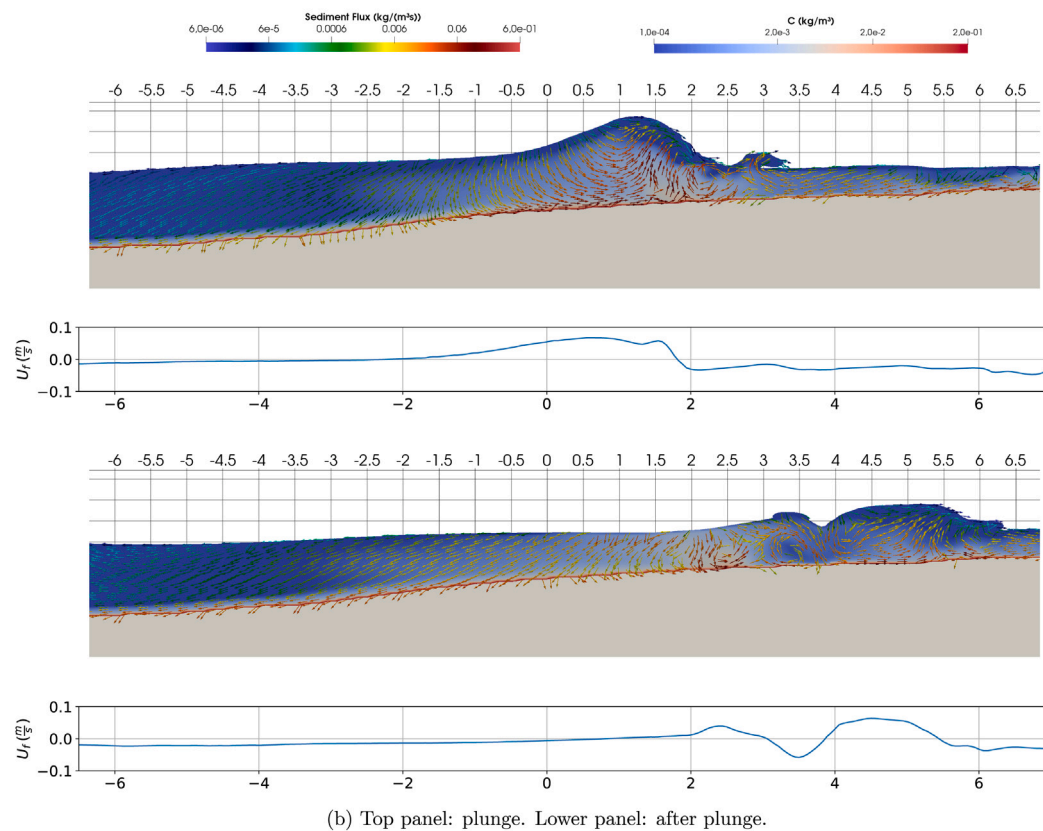
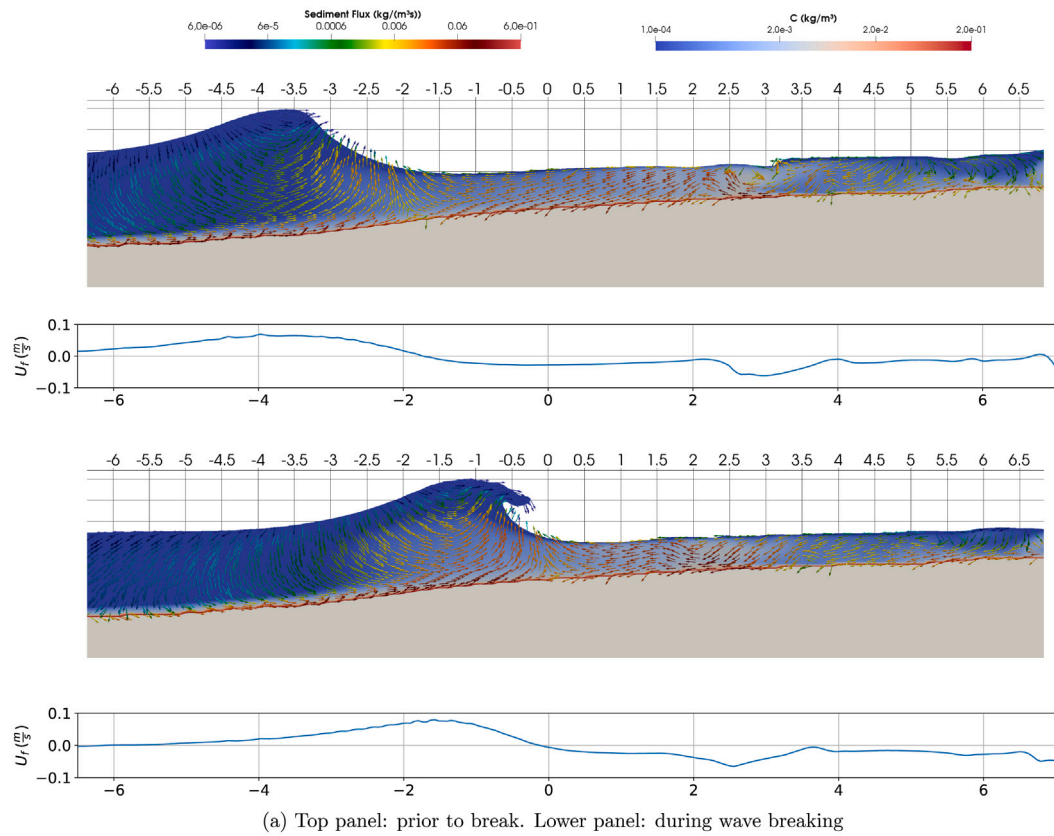


Fig. 13. Sediment flux and concentration during different stages of wave breaking. The instantaneous fields are obtained after 50 waves. Below each vector map, the instantaneous friction velocity is represented. Coloured arrows: sediment flux. Colour map: sediment concentration. Blue continuous line: friction velocity. (For interpretation of the references to colour in this figure legend, the reader is referred to the web version of this article.)

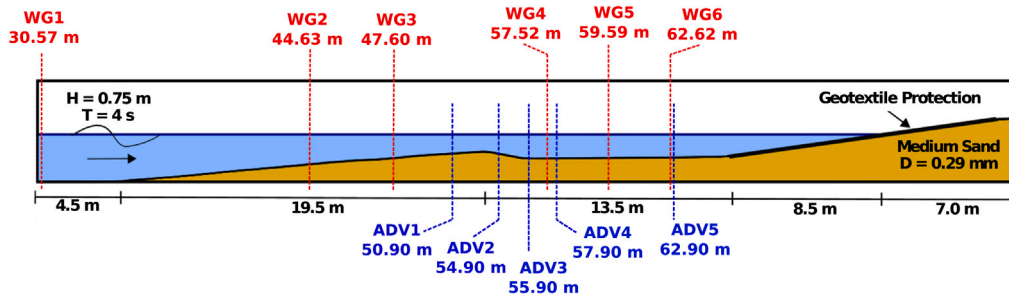


Fig. 14. Schematic view of the numerical domain and the position of sensors (wave gauges in red, ADVs in blue) which are used for the validation. The x position in the experiment to which they correspond is also indicated on each sensor for reference.

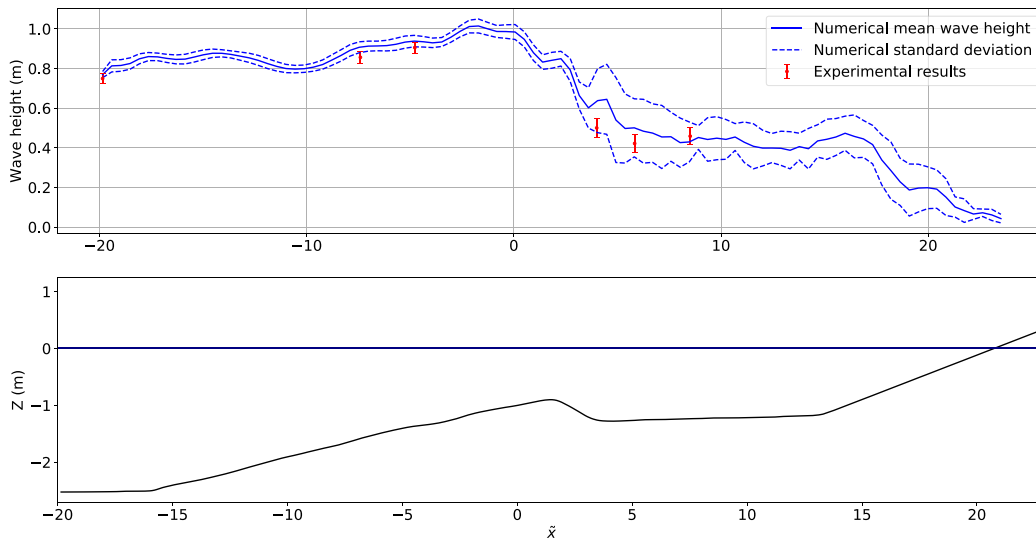


Fig. 15. Wave height at different locations along the experimental set-up for waves 50 to 100. Upper panel: wave height evolution along the profile. Bottom panel: initial seabed shape. Blue continuous line: numerical mean wave height. Blue dashed lines: standard deviation of numerical wave height. Red dots: experimental mean wave height. Red bars: standard deviation of the experimental wave height.

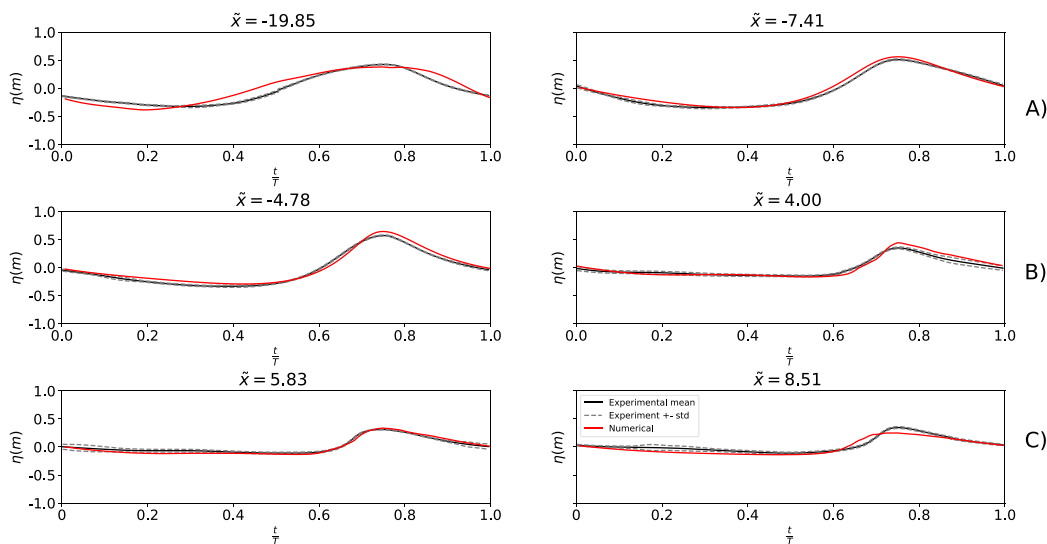


Fig. 16. Phase-averaged free surface. Red lines: Numerical results. Black continuous lines: experimental phase-averaged free-surface from van der Zanden et al. (2017b). Grey dashed lines: standard deviation of experimental free-surface. (For interpretation of the references to colour in this figure legend, the reader is referred to the web version of this article.)

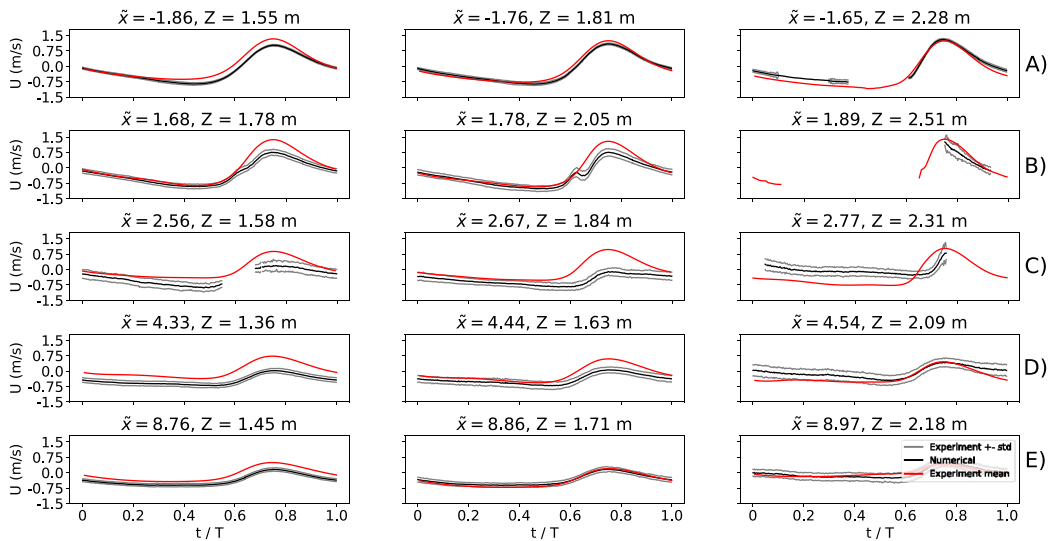


Fig. 17. Phase-averaged velocities. Red line: numerical model results. Black line: mean experimental results from van der Zanden et al. (2017b). Grey lines: standard deviation of experimental results. (For interpretation of the references to colour in this figure legend, the reader is referred to the web version of this article.)

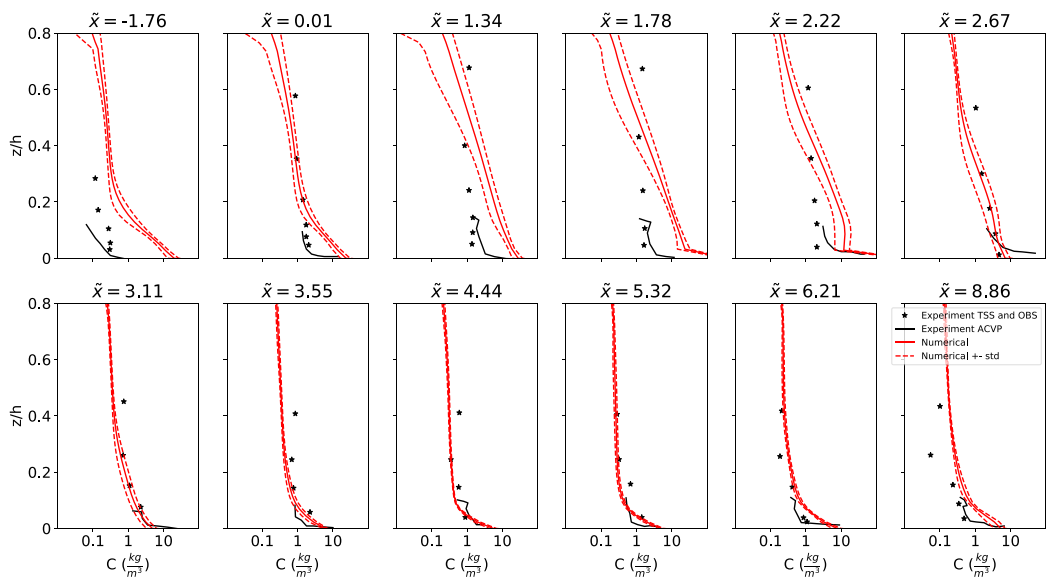


Fig. 18. Averaged concentration profiles at different positions. Red continuous lines: numerical results. Red dashed lines: standard deviation of the numerical results. Black stars: experimental data obtained from TSS and OBS measurements. Black lines: near-bed data from ACVP measurements.

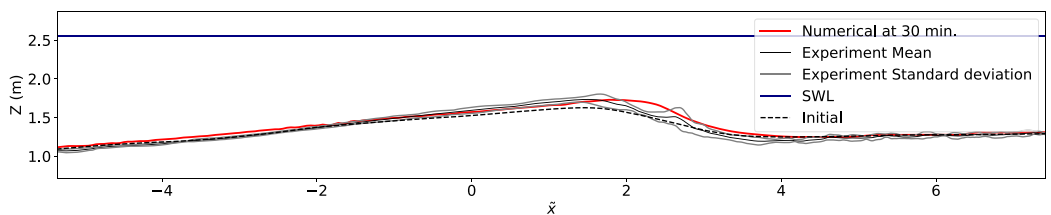


Fig. 19. Beach profile at after 30 min. Red line: numerical results. Black line: averaged experimental beach profile. Grey dashed lines: standard deviation of the experimental beach profile. (For interpretation of the references to colour in this figure legend, the reader is referred to the web version of this article.)

Furthermore, it does not include any calibration parameter or modifications of the empirical formulae used in it.

Validations show that the model is able to predict the morphological evolution of a complete beach profile under regular waves and erosive conditions, including the shoaling, surf and swash zones, in a satisfying manner.

The first validation case consists in comparing the tangential stresses induced by a solitary wave during its breaking process. Laboratory and numerical model provide similar results, being the largest differences in the run-down stage due to the difficulties in the simulation of the hydraulic jump.

Another two validation cases, in which the evolution of the beach profile is numerically reproduced, show consistent agreement between

experimental and numerical results. In the large-scale validation, the hydrodynamic magnitudes (wave height, shape and velocities) and the resulting seabed shape are well predicted by the model, a reasonable approximation of the concentration profiles has also been achieved. Overall discrepancies between experimental and numerical results can be due to the three-dimensional and air entrainment effects in the wave breaking process, the simplifications introduced by the empirical formulae, and differences between the exact conditions in which the tests were run regarding sediment properties, wave characteristics, and wave generation and absorption.

A remarkable reduction in the computational cost, which is approximately 10 times less than in previous RANS models, is attained. Additionally, the parallel version allows to run the simulations in even shorter times.

With sufficient precision and low computational cost, IH2VOF-SED facilitates the detailed analysis of different processes occurring in the cross-shore profile which are hard to measure in both laboratory and field, and excessively expensive to simulate with other RANS models. Therefore, it extends the ability to further investigate such processes and the interactions between them.

CRedit authorship contribution statement

J. García-Maribona: Conceptualization, Methodology, Software, Validation, Writing – original draft, Writing – review & editing. **J.L. Lara:** Conceptualization, Methodology, Writing - review & editing, Funding acquisition. **M. Maza:** Conceptualization, Writing – review & editing. **I.J. Losada:** Writing – review & editing.

Declaration of competing interest

The authors declare that they have no known competing financial interests or personal relationships that could have appeared to influence the work reported in this paper.

Acknowledgements

The writers are grateful to Iván Cáceres (Polytechnic University of Catalunya) and Tom Baldock (University of Queensland) for providing experimental data for the validation cases. Also, to Moisés Álvarez Cuesta for performing the XBeach simulations.

J. García-Maribona is indebted to the MECD (Ministerio de Educación, Cultura y Deporte, Spain) for the funding provided in the FPU (Formación del Profesorado Universitario) studentship (FPU17/04356).

M. Maza is sincerely grateful to the Spanish Ministry of Science, Innovation and Universities for the funding provided in the grant Juan de la Cierva Incorporación (BOE de 27/10/2017).

The work leading to this paper has been partially funded under the Retos Investigación 2018 (grant RTI2018-097014-B-I00) program of the Spanish Ministry of Science, Innovation and Universities.

Appendix A. Mass of sediment conservation analysis

To check whether a proper mass conservation is achieved or not, the total volume of sediment inside the domain is monitored. Fig. A.20 shows the total and suspended sediment volumes inside the numerical domain normalized with the initial total volume of sediment. The volumes have been obtained by integrating the sediment contained on each cell over the whole domain, also considering the amount that exits the domain through the wave generation boundary. As only a small part of the total sediment volume in the domain is mobilized by the hydrodynamics, the mass conservation is shown relative to the amount of sediment put into suspension. Accordingly, the vertical axis does not start at 0.

It can be observed that the total volume of sediment is constant along the simulation, therefore, a proper mass conservation has been achieved. The difference between total sediment and the sediment contained in the seabed is the suspended sediment. During the first seconds of simulation, a large erosion is generated increasing the total suspended volume in the domain. Oscillations in the total suspended sediment due to the wave breaking and other phenomena with larger time scales than the wave period can be noted.

Appendix B. Mesh sensitivity analysis

To analyse the influence of mesh discretization on the results, a mesh sensitivity analysis is performed for the medium-scale validation case. This case is selected for the sensitivity analysis as the seabed displacements are more noticeable than in the large-scale. The characteristics of the three meshes considered for this analysis are given in Table B.2, an aspect ratio of 2 is maintained for all of them.

The effect of mesh discretization on wave evolution along the profile is analysed. Fig. B.21 shows the results obtained for meshes described

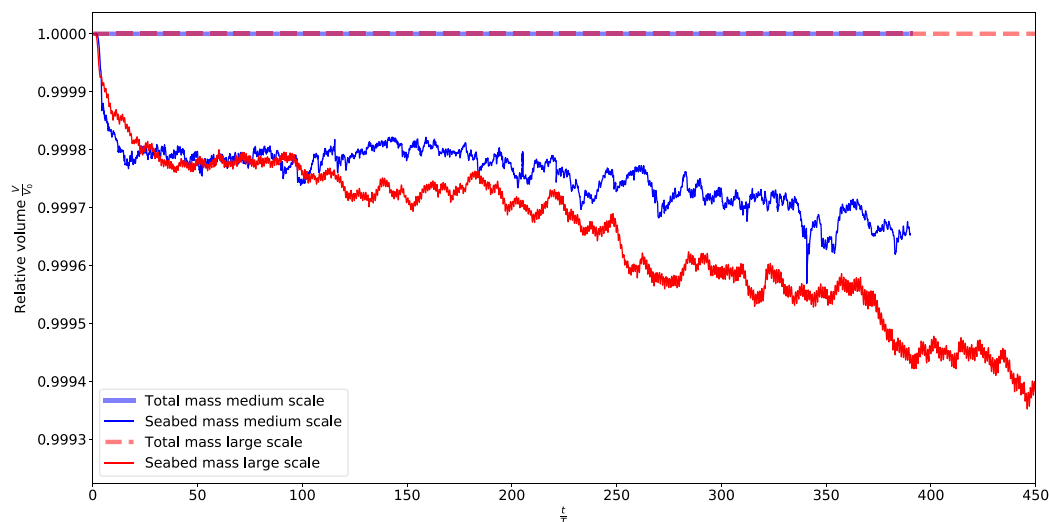


Fig. A.20. Mass conservation monitoring for the medium-scale (blue line) and large-scale (red line) simulations. In blue continuous and red dashed lines the total volume of sediment into the numerical domain for each validation case. (For interpretation of the references to colour in this figure legend, the reader is referred to the web version of this article.)

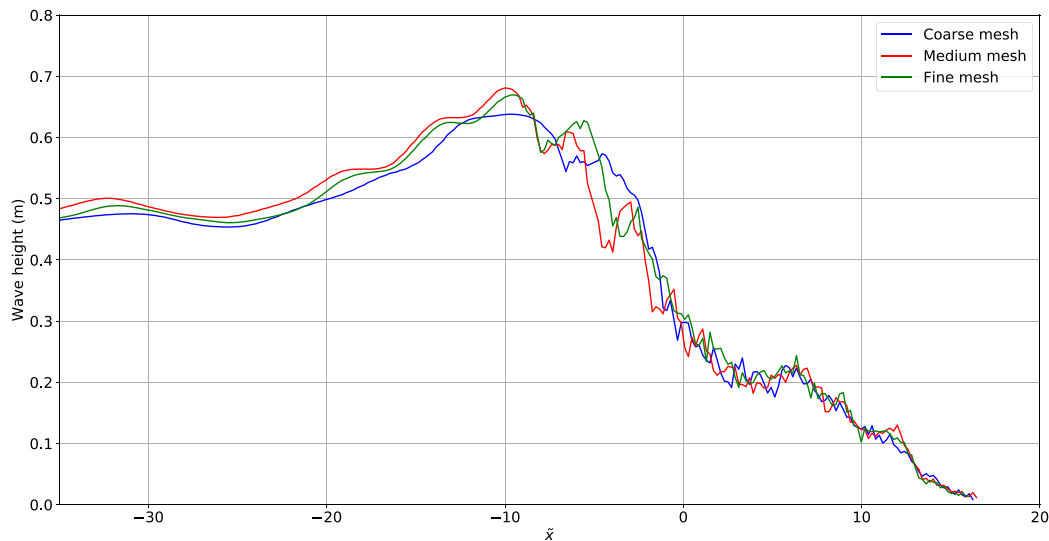


Fig. B.21. Wave height evolution along the domain for the three meshes described in Table B.2. Blue line: coarse mesh (H/20). Red line: medium mesh (H/22.5). Green line: fine mesh (H/25). (For interpretation of the references to colour in this figure legend, the reader is referred to the web version of this article.)

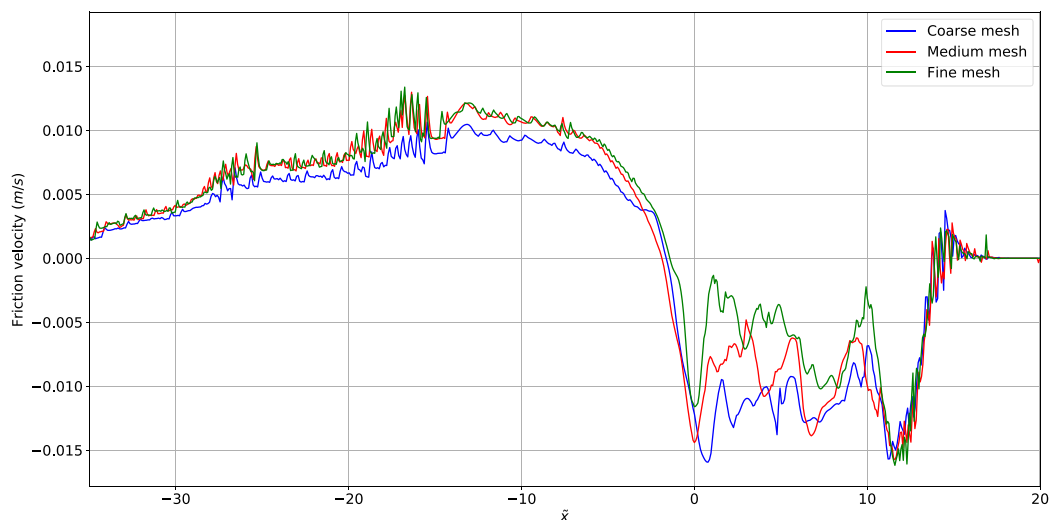


Fig. B.22. Time-averaged friction velocity evolution along the domain for the three meshes described in Table B.2. Blue line: coarse mesh (H/20). Red line: medium mesh (H/22.5). Green line: fine mesh (H/25). (For interpretation of the references to colour in this figure legend, the reader is referred to the web version of this article.)

Table B.2

Characteristics of the tested meshes.

Case	ΔY	ΔX	Cells	Computing time (1 core)
H/20	0.022	0.044	110,212	42 h
H/22.5	0.019	0.038	147,823	60 h
H/25	0.017	0.034	184,564	123 h

in Table B.2. The mean wave height has been obtained for waves 50 to 100.

Fig. B.21 reveals a small mesh dependency for the wave height evolution along the beach profile. In the shoaling and swash zones the results are very similar, while in the proximity of the breaking point and surf zone the differences are more noticeable. The sudden drop in wave height is produced at the same position in all cases. However, there are differences in the evolution of wave height seawards this point, especially for the coarse mesh.

The mesh discretization influence on friction velocity is shown in Fig. B.22. The time-averaged friction velocity has been obtained for waves 50 to 100.

Friction velocities are more sensitive to mesh discretization than wave height evolution, especially in the outer surf zone. The medium and fine meshes provide similar results for the shoaling and swash zones and the landwards part of the inner surf zone. Although the distribution of friction velocity obtained with the medium and fine meshes are similar in shape, the finer mesh gives smaller time-averaged friction velocities in the surf zone.

The friction velocity is more sensitive to the mesh discretization as not only the outer flow has to be resolved with sufficient resolution, but also the distance between the first non-solid cell and the seabed has to be small enough so that the assumed logarithmic profile for the boundary layer, used in (14), is applicable.

The successive reduction in mesh size results in a similar friction velocity distribution. The medium mesh (H/22.5) is used in the validation cases as it provides a good overall agreement with the experimental results at low computational cost, being therefore the one that better matches the objectives of this work.

References

- Amoudry, L.O., Hsu, T.J., Liu, P.L.-F., 2005. Schmidt Number and near-bed boundary condition effects on a two-phase dilute sediment transport model. *J. Geophys. Res. C: Oceans* 110 (9), 1–12.
- Bailard, J.A., Inman, D.L., 1981. An energetics bedload model for a plane sloping beach: Local transport. *J. Geophys. Res. Oceans* 86 (C3), 2035–2043.
- Balay, S., Abhyankar, S., Adams, M.F., Brown, J., Brune, P., Buschelman, K., Dalcin, L., Eijkhout, V., Gropp, W.D., Kaushik, D., Knepley, M.G., McInnes, L.C., Rupp, K., Smith, B.F., Zampini, S., Zhang, H., 2015a. PETSc Users Manual. Technical Report ANL-95/11 - Revision 3.6, Argonne National Laboratory.
- Balay, S., Abhyankar, S., Adams, M.F., Brown, J., Brune, P., Buschelman, K., Dalcin, L., Eijkhout, V., Gropp, W.D., Kaushik, D., Knepley, M.G., McInnes, L.C., Rupp, K., Smith, B.F., Zampini, S., Zhang, H., 2015b. PETSc web page. <http://www.mcs.anl.gov/petsc>.
- Balay, S., Gropp, W.D., McInnes, L.C., Smith, B.F., 1997. Efficient management of parallelism in object oriented numerical software libraries. In: Arge, E., Bruaset, A.M., Langtangen, H.P. (Eds.), *Modern Software Tools in Scientific Computing*. Birkhäuser Verlag, pp. 163–202.
- Baldock, T.E., Alsina, J.M., Cáceres, I., Vicinanza, D., Contestabile, P., Power, H., Sanchez-Arcilla, A., 2011. Large-scale experiments on beach profile evolution and surf and swash zone sediment transport induced by long waves, wave groups and random waves. *Coast. Eng.* 58 (2), 214–227.
- Baykal, C., Sumer, B.M., Fuhrman, D.R., Jacobsen, N.G., Fredsøe, J., 2015. Numerical investigation of flow and scour around a vertical circular cylinder. *Phil. Trans. R. Soc. A* 373 (2033), 20140104.
- Bruun, P., 1962. Sea-level rise as a cause of shore erosion. *J. Waterw. Harb. Div.* 88 (1), 117–132.
- Cáceres, I., Alsina, J.M., Sánchez-Arcilla, A., 2009. Mobile bed experiments focused to study the swash zone evolution. *J. Coast. Res.* 2009 (SPEC. ISSUE 56), 1736–1740.
- Capizzano, F., 2011. Turbulent wall model for immersed boundary methods. *AIAA J.* 49 (11), 2367–2381.
- Cheng, Z., Hsu, T.J., Calantoni, J., 2017. SedFoam: A multi-dimensional Eulerian two-phase model for sediment transport and its application to momentary bed failure. *Coast. Eng.* 119, 32–50.
- Dean, R.G., 1995. Cross-shore sediment transport processes. In: *Advances in Coastal and Ocean Engineering*. World Scientific, pp. 159–220.
- Farrell, P.E., Maddison, J.R., 2011. Conservative interpolation between volume meshes by local Galerkin projection. *Comput. Methods Appl. Mech. Engrg.* 200 (1), 89–100.
- Fredsøe, J., Deigaard, R., 1992. *Mechanics of Coastal Sediment Transport*. In: *Advanced Series On Ocean Engineering*, World Scientific Publishing Company.
- García, M., Parker, G., 1991. Entrainment of bed sediment into suspension. *J. Hydraul. Eng.* 117 (4), 414–435.
- Grasso, F., Michallet, H., Barthélemy, E., 2011. Experimental simulation of shoreface nourishments under storm events: A morphological, hydrodynamic, and sediment grain size analysis. *Coast. Eng.* 58 (2), 184–193.
- Grasso, F., Michallet, H., Barthélemy, E., Certain, R., 2009. Physical modeling of intermediate cross-shore beach morphology: Transients and equilibrium states. *J. Geophys. Res. Oceans* 114 (9), 1–15.
- Han, X., Lin, P., 2018. 3D numerical study of the flow properties in a double-spur dikes field during a flood process. *Water* 10, 1574.
- Hoefel, F., Elgar, S., 2003. Wave-induced sediment transport and sandbar migration. *Science* 299 (5614), 1885–1887.
- Hsu, T.J., Sakakiyama, T., Liu, P.L.-F., 2002. A numerical model for wave motions and turbulence flows in front of a composite breakwater. *Coast. Eng.* 46 (1), 25–50.
- Jacobsen, N.G., Fredsøe, J., Jensen, J.H., 2014. Formation and development of a breaker bar under regular waves. Part 1: Model description and hydrodynamics. *Coast. Eng.* 88, 182–193.
- Jara, M., González, M., Medina, R., 2015. Shoreline evolution model from a dynamic equilibrium beach profile. *Coast. Eng.* 99, 1–14.
- Kalligeris, N., Smit, P.B., Ludka, B.C., Guza, R.T., Gallien, T.W., 2020. Calibration and assessment of process-based numerical models for beach profile evolution in southern California. *Coast. Eng.* 158, 103650.
- Lara, J.L., Ruju, A., Losada, I.J., 2011. Reynolds Averaged Navier-Stokes modelling of long waves induced by a transient wave group on a beach. *Proc. R. Soc. A* 467 (2129), 1215–1242.
- Larsen, B.E., Fuhrman, D.R., 2018. On the over-production of turbulence beneath surface waves in Reynolds-averaged Navier–Stokes models. *J. Fluid Mech.* 853, 419–460.
- Larsen, B.E., Fuhrman, D.R., 2019. Full-scale CFD simulation of tsunamis. Part 1: Model validation and run-up. *Coast. Eng.* 151, 22–41.
- Larsen, B.E., Fuhrman, D.R., Sumer, B.M., 2016. Simulation of wave-plus-current scour beneath submarine pipelines. *J. Waterw. Port Coast. Ocean Eng.* 142 (5), 04016003.
- Larsen, B.E., van der A, D.A., van der Zanden, J., Ruessink, G., Fuhrman, D.R., 2020. Stabilized RANS simulation of surf zone kinematics and boundary layer processes beneath large-scale plunging waves over a breaker bar. *Ocean Model.* 155, 101705.
- Lesser, G.R., Roelvink, J.A., van Kester, J.A.T.M., Stelling, G.S., 2004. Development and validation of a three-dimensional morphological model. *Coast. Eng.* 51 (8–9), 883–915.
- Li, J., Qi, M., Fuhrman, D.R., 2019. Numerical modeling of flow and morphology induced by a solitary wave on a sloping beach. *Appl. Ocean Res.* 82, 259–273.
- Lin, P., Cheng, L., Liu, D., 2016. A two-phase flow model for wave–structure interaction using a virtual boundary force method. *Comput. & Fluids* 129, 101–110.
- Lin, P., Liu, P.L.-F., 1998. A numerical study of breaking waves in the surf zone. *J. Fluid Mech.* 359, 239–264.
- Losada, I.J., Lara, J.L., Guanche, R., Gonzalez-Ondina, J.M., 2008. Numerical analysis of wave overtopping of rubble mound breakwaters. *Coast. Eng.* 55 (1), 47–62.
- Martins, K., Blenkinsopp, C.E., Almar, R., Zang, J., 2017. The influence of swash-based reflection on surf zone hydrodynamics: a wave-by-wave approach. *Coast. Eng.* 122, 27–43.
- Miller, J.K., Dean, R.G., 2004. A simple new shoreline change model. *Coast. Eng.* 51 (7), 531–556.
- Mohd-Yusof, J., 1997. Combined immersed boundary/b-spline methods for simulations of flow in complex geometries. *Cent. Turbul. Res. Annu. Res. Briefs* 317–328.
- Nairn, R.B., Southgate, H.N., 1993. Deterministic profile modelling of nearshore processes. Part 2. sediment transport and beach profile development. *Coast. Eng.* 19 (1), 57–96.
- Okayasu, A., Katayama, H., 1992. Distribution of undertow and long-wave component velocity due to random waves. *Coast. Eng. Proc.* 1 (23).
- Rakha, K.A., Deigaard, R., Brøker, I., 1997. A phase-resolving cross-shore sediment transport model for beach profile evolution. *Coast. Eng.* 31 (1–4), 231–261.
- van Rijn, L.C., 1984. Sediment transport, part II: Suspended load transport. *J. Hydraul. Eng.* 110 (11), 1613–1641.
- van Rijn, L.C., Tonnon, P.K., Walstra, D.J.R., 2011. Numerical modelling of erosion and accretion of plane sloping beaches at different scales. *Coast. Eng.* 58 (7), 637–655.
- van Rijn, L.C., Walstra, D.J.R., Grasmeyer, B., Sutherland, J., Pan, S., Sierra, J.P., 2003. The predictability of cross-shore bed evolution of sandy beaches at the time scale of storms and seasons using process-based profile models. *Coast. Eng.* 47 (3), 295–327.
- Roelvink, D., Reniers, A., van Dongeren, A., van Thiel de Vries, J., McCall, R., Lescinski, J., 2009. Modelling storm impacts on beaches, dunes and barrier islands. *Coast. Eng.* 56 (11–12), 1133–1152.
- Roulund, A., Sumer, B.M., Fredsøe, J., Michelsen, J., 2005. Numerical and experimental investigation of flow and scour around a circular pile. *J. Fluid Mech.* 534, 351–401.
- Ruju, A., Lara, J.L., Losada, I.J., 2012. Radiation stress and low-frequency energy balance within the surf zone: A numerical approach. *Coast. Eng.* 68, 44–55.
- Smith, J.D., McLean, S.R., 1977. Spatially averaged flow over a wavy surface. *J. Geophys. Res.* 82 (12), 1735–1746.
- Southgate, H.N., Nairn, R.B., 1993. Deterministic profile modelling of nearshore processes. Part 1. Waves and currents. *Coast. Eng.* 19 (1), 27–56.
- Stive, M.J.F., 1986. A model for cross-shore sediment transport. *Coast. Eng. Proc.* 1 (20), 114.
- Sumer, B.M., Guner, H.A.A., Hansen, N.M., Fuhrman, D.R., Fredsøe, J., 2013. Laboratory observations of flow and sediment transport induced by plunging regular waves. *J. Geophys. Res. Oceans* 118 (11), 6161–6182.
- Sumer, B.M., Sen, M.B., Karagali, I., Ceren, B., Fredsøe, J., Sottile, M., Zilioli, L., Fuhrman, D.R., 2011. Flow and sediment transport induced by a plunging solitary wave. *J. Geophys. Res. Oceans* 116 (1), 1–15.
- Sun, R., Xiao, H., 2016. SediFoam: A general-purpose, open-source CFD–DEM solver for particle-laden flow with emphasis on sediment transport. *Comput. Geosci.* 89, 207–219.
- Ting, F.C.K., Kirby, J.T., 1994. Observation of undertow and turbulence in a laboratory surf zone. *Coast. Eng.* 24 (1), 51–80.
- Ting, F.C.K., Kirby, J.T., 1995. Dynamics of surf-zone turbulence in a strong plunging breaker. *Coast. Eng.* 24 (3), 177–204.
- Torres-Freyermuth, A., Losada, I.J., Lara, J.L., 2007. Modeling of surf zone processes on a natural beach using Reynolds-averaged Navier–Stokes equations. *J. Geophys. Res. Oceans* 112 (C9).
- Wilcox, D.C., 1998. *Turbulence Modelling for CFD*. DCW Industries.
- Wright, L.D., Short, A.D., 1984. Morphodynamic variability of surf zones and beaches: A synthesis. *Mar. Geol.* 56 (1), 93–118.
- Yates, M.L., Guza, R.T., O'Reilly, W.C., 2009. Equilibrium shoreline response: Observations and modeling. *J. Geophys. Res. Oceans* 114 (C9).
- van der Zanden, J., van der A, D.A., Hurther, D., Cáceres, I., O'Donoghue, T., Hulscher, S.J.M.H., Ribberink, J.S., 2017b. Bedload and suspended load contributions to breaker bar morphodynamics. *Coast. Eng.* 129 (April), 74–92.
- van der Zanden, J., van der A, D., Hurther, D., Cáceres, I., O'Donoghue, T., Ribberink, J.S., 2017a. Suspended sediment transport around a large-scale laboratory breaker bar. *Coast. Eng.* 125, 51–69.